Experimental Study on Fast Ion Losses in the Compact Helical System

Takashi Kondo

Doctor of Philosophy

Department of Fusion Science
School of Mathematical and Physical Science
The Graduate University for Advanced Studies

1999

Abstract

In magnetic confinement devices, it is required that fast ions, such as heating ions and alpha particles, are well confined until they transfer their energy to plasmas. In order to understand loss processes and loss mechanisms of fast ions in magnetic confinement devices, direct measurements of escaping fast ions are essential. These studies have been advanced on large tokamaks experimentally and theoretically. On heliotron/torsatron devices which are regarded as alternative devices of tokamaks, it is especially important to study loss processes and loss mechanisms because fast ion orbits in heliotron/torsatron devices are complicated due to the presence of helical ripples in addition to toroidal ripples.

In this study, a scintillator-type lost-fast-ion probe has been used for the first time to measure escaping fast ions originated from a tangentially injected neutral beam (NB) on the Compact Helical System (CHS) heliotron/torsatron. The probe detects escaping fast ions directly in the vacuum vessel and can provide the information on the pitch angle χ and the gyroradius ρ_i corresponding to the energy of detected ions. The probe mainly consists of a scintillator plate (ZnS(Ag)), an image-intensified CCD camera and a nine channel fiber array coupled each with a photomultiplier tube (PMT). The probe head (detection point) is placed at the distance of a few cm away from the last closed magnetic surface. Positions on the scintillator plate struck by incident escaping fast ions have the information on χ and ρ_i. The time behaviors of escaping fast ions with different ranges of χ and ρ_i are obtained by using the PMT array with the time resolution of 50 μs. A χ-ρ_i profile, light spots on the scintillator, are obtained by the CCD camera as a 2D image with the time resolution of 33.3 ms (30 Hz). The probe has a Faraday cup structure. The total absolute flux of ions incident on the scintillator can be measured as ion current. Prior to measurements, calibration works for the gain characteristic of instruments were made to compare the signal intensity among each of plasma discharges measured with different gain of these instruments or each of PMTs.

Loss orbits are identified by using an orbit following code with measured information on the pitch angle and the energy. Orbits are simply derived by solving

the equation of motion with Lorentz force. Orbits start from the detector position and are calculated backwards in time.

The measurement was applied to NB heated plasmas on CHS. First of all, it was inspected that the probe signal does not arise from X-rays, the leakage of plasma lights and other noises, but from escaping beam ions. As a feature of the signal, the signal was observed just during NB injection and the signal intensity increased as the magnetic axis position R_{ax} moved outward (plasmas come close to the probe). Light spots on the scintillator moved to the position predicted from the magnetic field strength at the probe position with changes of the toroidal magnetic field strength B_T.

The fast measurement is essential for the investigation of time behaviors of escaping fast ions. Three kinds of losses were observed and were identified as losses from passing, transition and trapped orbits. The different time behaviors of escaping ions, which suggest different classical loss processes, were observed on signals corresponding to passing ions and trapped ions. The signal of passing ions started synchronously at the moment of NB injection, while the signal intensity of trapped ions rose gradually in time. To reveal these loss processes, the dependence of the rise time behavior for both signals on the electron density n_e was investigated. The signal intensity of passing ions always rapidly increased with NB injection, independently of n_e. On the other hand, the rise time of trapped ion signal was inversely proportional to n_e and showed similar tendency to that of the calculated deflection time. Therefore, it is thought that the former is due to the prompt loss and the latter is due to the collisional pitch angle scattering loss depending on n_e.

The fast measurement was applied to NB-heated plasmas with fishbone-like instabilities and toroidicity-induced Alfven eigenmode (TAE). In CHS, two types of the fishbone-like instabilities were observed on Mirnov coil array, soft-X ray array and a heavy ion beam probe. One is the m/n =3/2 (m/n =poloidal/toroidal mode number) fishbone-like instability, which is often observed in a discharge with an outward-shifted plasma ($R_{ax} \geq 0.949$ m). The other is the m/n=2/1 fishbone-like instability, which is often observed in a discharge with an inward-shifted plasma (R_{ax}=0.921 m). The low magnetic field (B_T~0.9 T), the co-injected NB and the low n_e (n_e~1.0×10^{19} m^{-3}) are characteristics of these two burst modes. No such instabilities were observed on

electron cyclotron resonance heated plasmas without NB injection. The periodic beam ion losses correlating with MHD oscillation were observed on the signals of co-going passing boundary ions and counter (ctr.)-going trapped ions with the energy lower than injection energy during the m/n=3/2 fishbone like instability. There were thresholds in the mode amplitude for the ejection of fast ions. Above the threshold, losses were enhanced with increase of the mode amplitude. The excitation of the fishbone-like instability and the enhancement of MHD-induced losses strongly depend on the degree of the accumulation of beam ions in plasmas. Orbit calculations show that passing boundary ions which have large pitch angle and the toroidal velocity close to zero or close to the propagating velocity of magnetic fluctuation near the m/n=3/2 surface are ejected by the instability. No MHD-induced losses were seen in plasmas with the m/n=2/1 fishbone-like instability or TAE.

In conclusion, direct measurements of escaping fast ions have been carried out in CHS and the classical loss processes (the prompt loss and the collisional pitch angle scattering loss) and the loss mechanism of MHD-induced loss were studied. In classical losses, the signal intensity of passing boundary ions was most intense. With regard to the loss mechanism of MHD-induced losses, it was found that passing boundary ions moving excursively across magnetic surfaces between the outside and the inside of a plasma have resonance points near the m/n=3/2 surface, where their toroidal velocity is close to zero or close to the propagating velocity of magnetic fluctuation. Therefore, it is necessary for future large devices to control passing boundary ions.

Acknowledgements

The author wishes to express special thanks to Prof. M. Sasao of National Institute for Fusion Science (NIFS) for her useful and continuous discussions and advices on this work. The author would like to thank Dr. M. Isobe of NIFS for his many useful suggestions and encouragements all over this work. The author is indebted to Dr. D. S. Darrow of Princeton Plasma Physics Laboratory for his useful supports and valuable discussions on this study. The author thanks Prof. A. Kitamura of Kobe Univ. of Mercantile Marine to give me the opportunity of this study at NIFS.

The author acknowledges the experimental support by Prof. K. Matsuoka and all members of the CHS group. The author wishes to thank Prof. K. Toi, Dr. M. Takechi and Mr. G. Matsunaga for providing data from magnetic probe measurements and valuable suggestions. The author thanks Dr. M. Osakabe for his supports on orbit calculations. The author also thanks Mr. C. Takahashi for his supports on CHS data acquisition.

The author acknowledges the encouragement given by Dr. M. Nishiura, Mr. Y. Liang, Mr. H. Sasao, Mr. Y. Nakahara, Dr. K. Ikeda, Dr. K. Tsuzuki, Dr. S. Inagaki, Dr. Y. Hasegawa, Dr. K. Hosaka, Dr. T. Kenmotsu, Dr. T. Imai, Mr. T. Kobuchi, Mr. Y. Shirai, Mr. K. Matsushita, Mr. T. Kuroda, Mr. K. Hirose, Mr. N. Mizuguchi, Mr. K. Ohkuni, Ms. N. Ashikawa, Mr. N. Tamura and the members of R&D group at NIFS.

The author is grateful for desk works managed by the official staff; Ms. S. Urushihara and Mr. T. Kondo, who are in charge of Grad. Univ. for Advanced Studies at NIFS.

The author would like to appreciate financial supports of the Japan Foundation Scholarship and the Fusion Science Association.

Contents

Chapter 1

Introduction

1.1 Overview

Thermonuclear fusion is thought to be a promising method providing energy for future. It is necessary that high temperature plasmas, reaching around 10 keV, are well confined by magnetic fields to sustain fusion reactions in plasmas. Toroidal magnetic confinement devices (tokamaks and stellarators including heliotron/torsatron devices) are considered as a candidate for fusion reactors [1,2]. To increase the plasma temperature, neutral beam injection (NBI) is widely used as a powerful heating method. Injected energetic neutral beams are deposited in plasmas and the energy of beam ions is transferred to bulk plasmas through collisions during circulation in a torus. Acceleration by ion cyclotron range of frequency heating (ICRF) is also used as a heating method. Energetic ions are created by fusion reactions, except these additional heating. Fusion products like 3.5 MeV alpha particles are important heating source to accomplish the self-ignition plasma in future fusion reactors. In magnetic confinement devices, it is required that fast ions, such as beam ions and alpha particles, are well confined until they transfer their energy to plasmas. Poor confinement of fast ions leads to a degradation of the heating efficiency. Plasma performance also deteriorates due to an influx of impurities sputtering caused by ejected fast ions striking the first wall. In order to avoid these problems, it is essential to study the fast ion loss behavior / mechanism. Such studies have been advanced on large tokamaks in both experiment and theory [3,4]. It is necessary to study loss processes and loss mechanisms especially on heliotron/torsatron devices, which are regarded as alternative devices of

tokamaks, because fast ion orbits in heliotron/torsatron devices are complicated due to the presence of helical ripples in addition to toroidal ripples.

In this study, a scintillator-type lost-fast-ion probe [5-18] has been used for the first time to measure escaping fast ions originating from a tangential NBI on the Compact Helical System (CHS) heliotron/torsatron. The probe detects escaping fast ions directly in the vacuum vessel and can provide the information on the pitch angle χ and the gyroradius ρ_i corresponding to the energy of detected beam ions. Loss orbits are identified by using an orbit following code with measured pitch angle and energy. The time behaviors of escaping fast ions with different ranges of χ and ρ_i are investigated with the fast measurements as a feature of this probe and the experimental study on fast ion losses are made.

This thesis is organized into six chapters. Fast ion orbits in CHS and orbit calculation codes are introduced in chapter 2. The experimental set-up including calibration works of instruments is described in chapter 3. Experimental results of measurements for classical losses, MHD-induced losses and other enhanced losses are presented in chapter 4. In chapter 5, the estimation of classical losses is made and the loss mechanisms of MHD-induced losses are discussed. Finally, the thesis concludes with chapter 6.

1.2 Loss processes of fast ions

Studies on fast ion losses have been advanced on large tokamaks in experiment and theory as mentioned in previous section. In this section, a part of these studies are introduced briefly.

Fast ions are lost by processes, such as prompt loss [7,13], toroidal field (TF) ripple loss [19-21], ICRF-induced loss [17] and magnetohydrodynamic (MHD)-induced loss [12]. Prompt loss is due to ions created in the loss cone. Therefore, these ions are lost immediately as soon as they are born. TF ripple loss is due to the ripple of magnetic fields because of the finite number of toroidal coils in tokamaks. Fast ions with large perpendicular velocity component trapped in the region between toroidal

coils move vertically due to ∇B drift because these trapped ions can not feel well the rotational transform and then they hit the first wall. ICRF waves accelerate the perpendicular velocity of resonant ions. The pitch angle of these ions is increased and passing ions move into the loss cone. MHD instabilities are often accompanied by redistribution and/or loss of fast ions. Especially MHD instabilities such as the fishbone instability or toroidicity-induced Alfven eigenmode (TAE) are excited by the presence of fast ions and can result in a perturbation to the fast ion population. The fishbone instability was first observed on the PDX tokamak in 1983 [22]. Fast ion losses during fishbones were studied by neutron measurements using a scintillator counter in 1984 [23]. Sudden drops in the neutron count during fishbones were observed, indicating fast ion loss. Similarly, studies have been widely done using Mirnov probes, soft-X ray array, neutron detectors and neutral particle analyzers [24,25]. Scintillator-type lost-fast-ion probes designed to measure fusion products were used to study the MHD-induced loss on the TFTR tokamak [12]. It was observed that losses were increased by up to a factor of 3 ~ 5 above the base loss level during MHD activity. Larger MHD-induced losses were seen when the neutral beam injection (NBI) power and the plasma current were increased in supershots.

1.3 Compact Helical System

The Compact Helical System is a heliotron/torsatron type device with a major radius R=1 m, an average minor radius $<a>$=0.2 m and a poloidal period number l=2 and a toroidal period number M=8 (Table 1) [26]. Figure 1 shows the magnetic surface of CHS. The maximum toroidal magnetic field at R=1 m, B_T is 2 T. In the standard operation mode, the direction of B_T is counterclockwise (ccw) as seen from above. The rotational transform, $\iota/2\pi$ increases from approximately 0.3 at the center to 1 at the last closed magnetic surface (LCMS) and the radial profiles of $\iota/2\pi$ depend on the magnetic axis position, R_{ax} and the beta value β as shown in Fig. 2. CHS has two electron cyclotron resonance frequency heating (ECRH) systems set at frequencies of 53 GHz and 106 GHz and two NBI systems; one (NBI #1) is oriented for co-injection

with a power of 1 MW gapped at 38 kV and the other (NBI #2) is oriented for counter (ctr) -injection and capable of delivering a power of 0.6 MW with a primary energy of 36 kV. An ion Bernstein wave system also has been installed for plasma formation and start-up.

Major diagnostics for fusion plasmas [27,28] are installed on CHS as shown in Fig.3. The line averaged electron density n_e is measured by an HCN interferometer and electron density and temperature profiles are measured using an YAG Thomson scattering system. The ion temperature is measured by a charge exchange recombination spectroscopy system, a neutral particle analyzer and neutron detectors. The Mirnov coil array, which has frequency response of up to ~200 kHz, is installed in the poloidal and toroidal direction on the first wall to determine poloidal/toroidal mode numbers (m/n) of the magnetic fluctuation [29, 30]. The global confinement property of neutral beam-injected fast ions has been investigated by means of neutron diagnostics and the neutral particle analyzer in CHS [31].

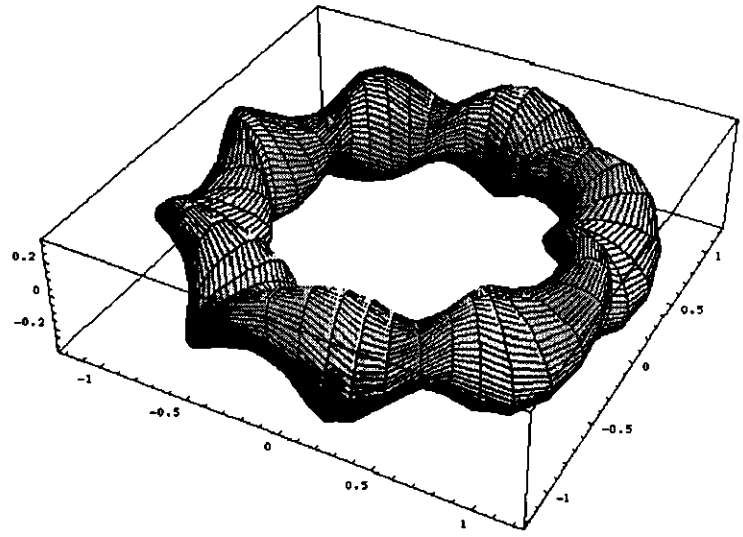

Fig. 1. Magnetic surface of CHS.

Table 1. Device parameters of CHS

Parameter	*Value*
Major radius, R	1 m
Averaged minor radius, $\langle a \rangle$	0.2 m
Aspect ratio, $R/\langle a \rangle$	5
Poloidal period number, l	2
Toroidal period number, M	8
Magnetic field strength, B_T	2T

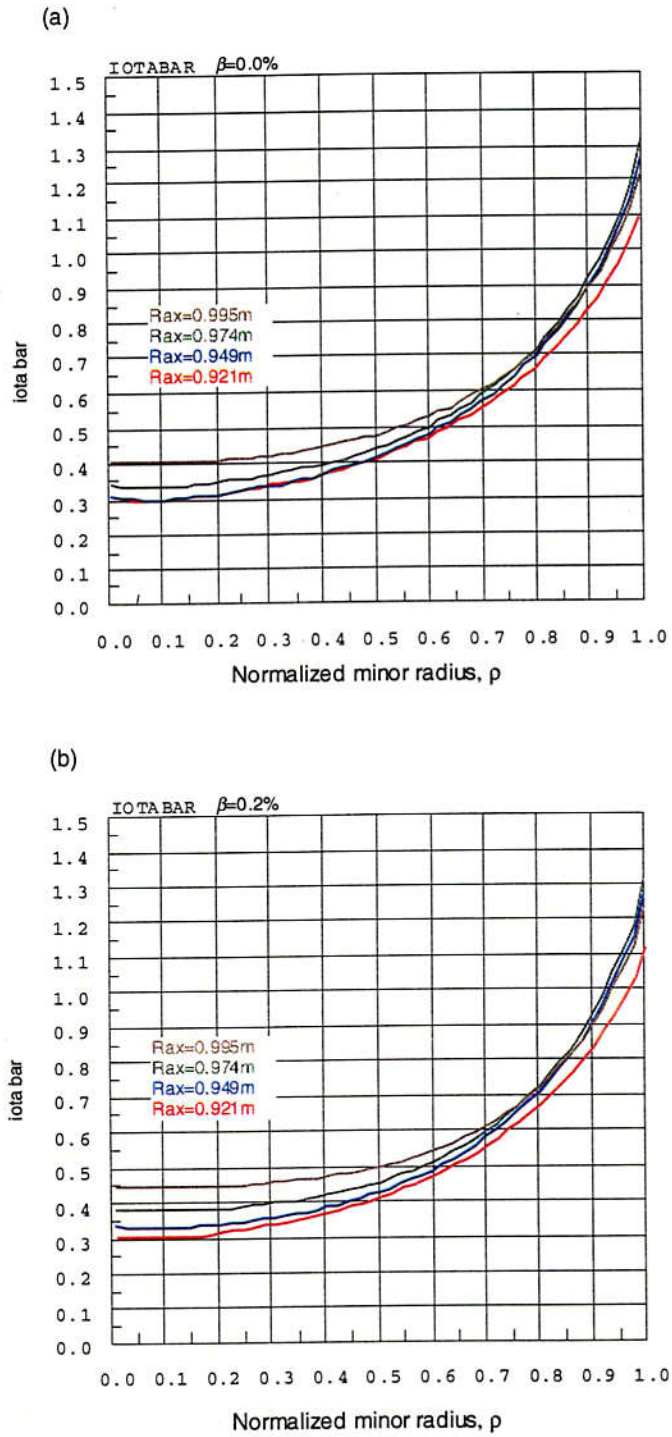

Fig. 2. Rotational transforms of CHS, (a) β=0.0% and (b) β=0.2%.

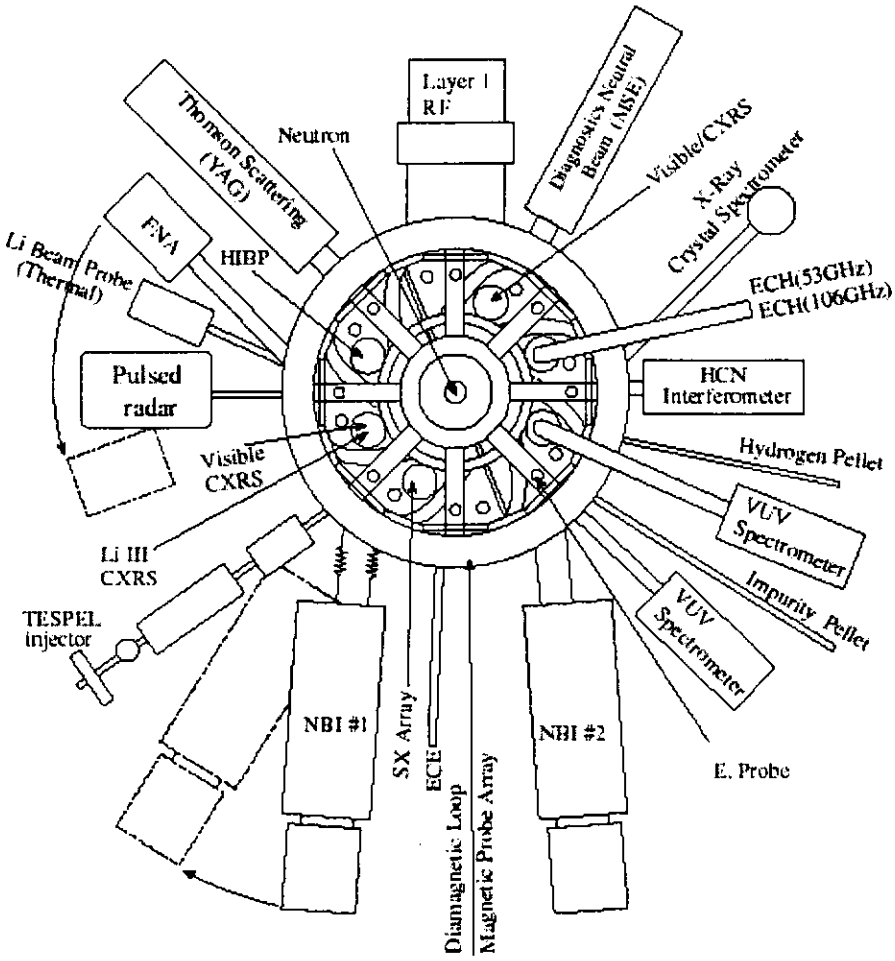

Fig. 3. Diagnostics on CHS.

Chapter 2

Fast ion orbits in CHS

2.1 Introduction

To study the single ion behavior in magnetic fields under the collisionless assumption is essential to the estimation of fast ion losses. For a single ion moving in magnetic fields in a torus, adiabatic invariants, the magnetic moment μ and the longitudinal adiabatic invariant J, are generally conserved. They are defined by following formula,

$$\mu = \frac{\frac{1}{2} m_i v_\perp^2}{B} \tag{1}$$

$$J = \oint v_{//} dl \tag{2}$$

where m_i, $v_\perp$ and B in Eq. (1) are mass, perpendicular velocity component of an ion and magnetic field strength, respectively. The integral is taken over the periodic orbit and $v_{//}$, dl are parallel velocity component and an element along a field line. Particle orbit forms closed drift surface because of the presence of these conserved quantities. Deviation of drift surface from magnetic surface is an important quantity about the confinement and behavior of fast ions. Fast ion orbits are classified by the type of drift surfaces as mentioned in section 2.3. The behavior of fast ions in helical magnetic fields is complicated and generally depends on many parameters, aspect ratio, magnetic field strength, pitch parameter of magnetic fields, helical ripples, beta value, energy and pitch angle of fast ions and electric field in plasmas. In section 2.2, an orbit following code used in this study to investigate the loss of fast ions with the complicated behavior on CHS is introduced.

2.2 Orbit calculation code

An orbit calculation code, developed by Heidbrink for tokamaks, was modified to simulate the motion of fast ions in the magnetic field of CHS [32,33]. The magnetic field of CHS is calculated with currents of the external coils with the method of multi filaments using the Biot-Savart law. Here the effect of plasma pressure is not taken into account, because the beta value is less than 0.2%, through the present work.
An orbit is derived from solving the following equation,

$$m_i \frac{dv}{dt} = q_i(v \times B) \qquad (3)$$

which is simply the Lorentz force law with electric field E=0 assumed. Here, v and q_i are velocity and charge of an ion, respectively. Orbits start from the detector position and are calculated backwards in time. The calculation follows the full gyro-orbit under the collisionless assumption as particle are highly non-adiabatic, *i.e.* ρ_i/L_B is large, where L_B is magnetic field scale length. When an ion strikes the first wall, the tracking calculation is stopped.

In CHS the radial profile of electrostatic potentials is directly measured with heavy ion beam probes (HIBP) [34]. For low density NBI plasmas (n_e~8 x 10^{12} m^{-3}), a parabolic potential profile with a negative central value of approximately -200 V is typically observed. This profile corresponds to the radial electric field ranging from approximately 0 to -20 V/cm. An orbit calculation including a radial electric field, which was developed by Osakabe, was performed to investigate the influence of electric field on fast ion orbits. An orbit is derived from solving the equation of the Lorentz force law adding just a term of radial electric field on the right hand side of Eq. (3). The radial potential profile as a function of the normalized minor radius ρ is given in the code as follows,

$$\Phi(\rho) = \Phi_0(1-\rho^2) \qquad (4)$$

where Φ_0 is a potential at the center of plasmas. Radial electric field of each point on an orbit is estimated from potentials of these points by an 1D finite difference method on ρ. Figure 4 shows the variation of positions of an ion with the energy E_i of (a)40

keV, (b)20 keV and (c)5keV and the pitch angle χ of 180° at the start point of R=1.0 m, toroidal angle ϕ=22.5° (horizontally elongated cross section) and vertical position z=0.0 m (midplane). The pitch angle χ is given by $\chi=\cos^{-1}(v_{//}/v)$. These calculations were performed for the magnetic field configuration of R_{ax}=0.921 m and B_T=0.9 T. The blue and red lines show the calculation with Φ_0=0 and -200 V, respectively. For the ions moving in the region of ρ<0.6 with these energies, differences in ρ between the calculations with Φ_0=0 and -200 V are not seen. Figure 5 shows the case of an ion with large movement in ρ (0.3<ρ<0.8); inside and outside of the plasma at the start point of R=1.1 m, ϕ=22.5° and z=0.0 m. In this case, no large difference in ρ between the calculations with Φ_0=0 and -200 V is seen. Figure 6 shows the calculations with Φ_0=0, -200 and -400 V for ions with E_i of 20 keV and χ of 105° at same start point in Fig. 4. Less variation of ρ ("amplitude") between the calculations with Φ_0=0, -200 V are seen for approximately 1 ms, while the calculation with Φ_0=-400 V is stopped because the ion moves to out of the plasma (ρ>1) as soon as the calculation was started (after 50 μs). From these results (Figs. 4-6), it was found that the influence of E in CHS on fast ions treated in this thesis is negligibly small. Therefore orbit calculations have been done under the assumption of E=0 through out for this study.

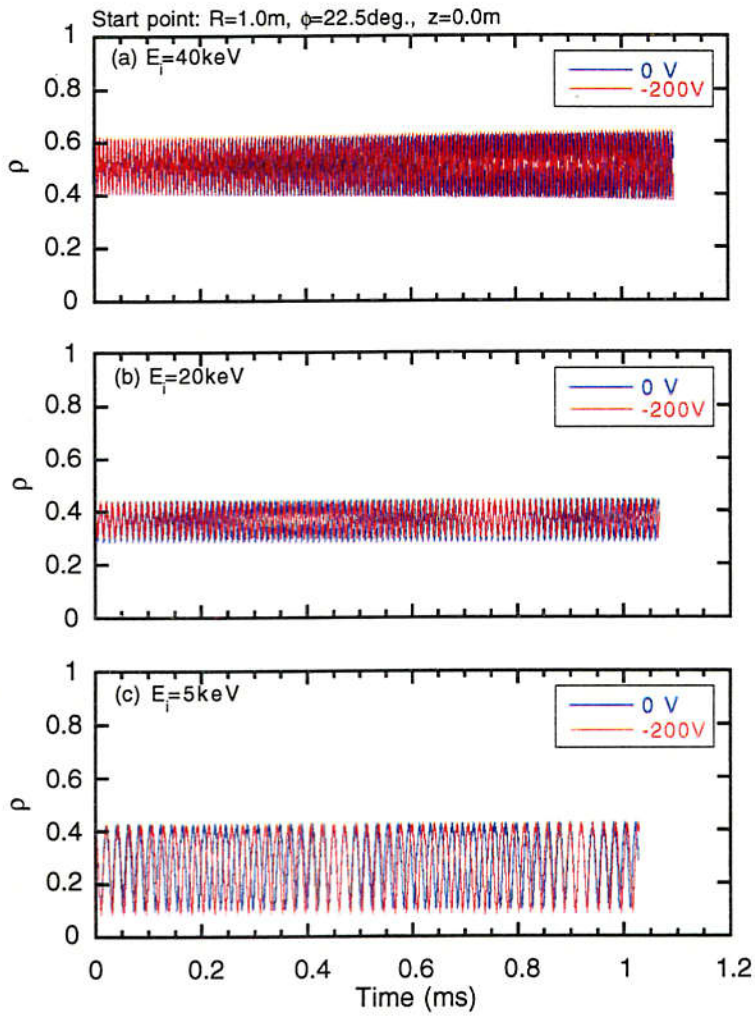

Fig. 4. Variation of positions of an ion with E_i of (a)40 keV, (b)20 keV and (c)5keV and χ of 180° for Φ_0=0 and -200 V. Differences in ρ between the calculations for Φ_0=0 and -200 V are not seen.

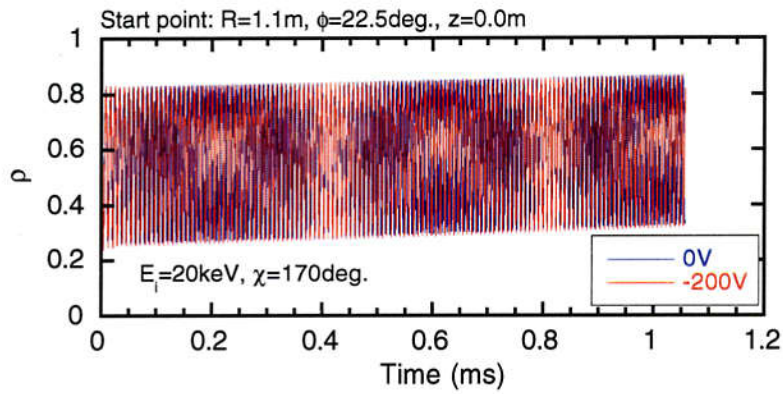

Fig. 5. Variation of positions of an ion moving inside and outside of the plasma largely with E_i of 20 keV and χ of 170° for Φ_0=0 and -200 V. Differences in ρ between the calculations for Φ_0=0 and -200 V are not seen.

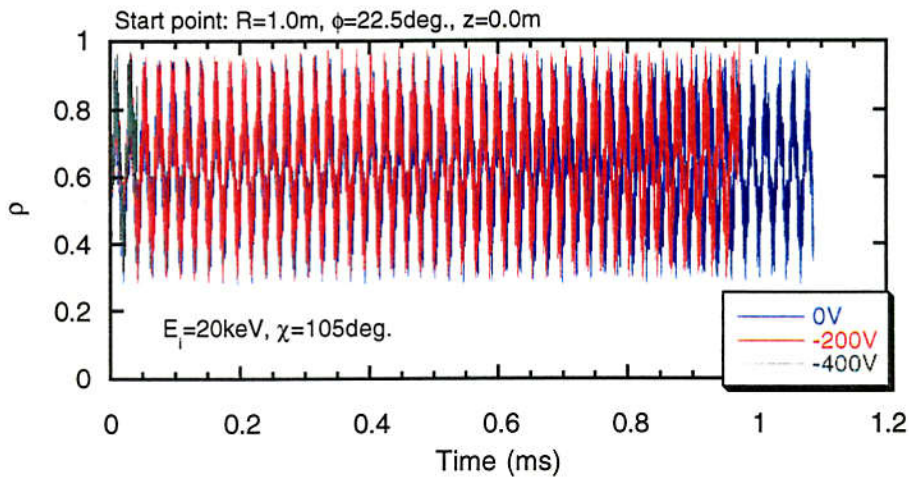

Fig. 6. Variation of positions of an ion with E_i of 20 keV and χ of 105° for Φ_0=0, -200 and -400 V. Variation of ρ between the calculations with Φ_0=0, -200 V is not seen, while the calculations with Φ_0=-400 V are different from that with Φ_0=0 V.

2.3 Classification of fast ion orbit

The magnetic fields of heliotron/torsatron type devices have helical ripple in addition to toroidal ripple and fast ions in helical magnetic fields are categorized as the followings: "passing ions", "local mirror trapped ions", "helically trapped ions" and "transition ions" [35]. Passing ions have a large pitch angle away from 90°, i.e. a large velocity component along the field line and continue to circulate along the field lines. Ions having a small velocity component along the field line are trapped by the magnetic mirror and are known as toroidal mirror trapped ions. Local mirror trapped ions have a bounce motion in the local mirror of the helical magnetic fields and move in a limited region toroidaly. Heliotron/torsatron type devices have a magnetic field ripple as called the helical ripple. Ions trapped by the helical ripple are called helically trapped ions. They circulate around the torus with a bounce motion in the helical ripple region. There is also a group of ions located near to the boundary of these three categories. They are reflected in the strong magnetic field region, and circulate in the weak field region. These ions have transition characteristics shared by passing orbits, helical trapped orbits and local mirror trapped orbits. Such ions are known as transition ions, or trapped/detrapped ions.

To investigate the fast ion behavior and to classify the types of fast ion orbits in CHS, orbit calculations were performed in the magnetic field configuration of R_{ax}=0.974 m and B_T=0.9 T. Ions with E_i of 10 keV were launched from the midplane of horizontally elongated cross section for R = 0.75, 0.80, 0.90 and 1.10 m with changing χ as shown in Figs. 7-10, respectively. Figures of the right column in Figs. 7-10 present toroidal views projected on the midplane, and those of the left one are poloidal projections of orbits. A circle in the poloidal projection is the locus of the longer radius of the elliptical shaped poloidal cross section. Figure 7 shows the behavior of fast ions launched from the inside of device (R =0.75 m). An ion with χ of 90° (Fig. 7(a)) has a helically trapped orbit and hits the first wall. An ion with χ of 100° (Fig. 7(b)) has a transition orbit between helically trapped orbits and passing orbits and continues to circulate with changing orbits in the torus. An ion with χ of 150° (Fig.

7(c)) has a passing orbit and is not lost. Figure 8 shows the case of R=0.80 m, which is rather out position from R=0.75 m. An ion with χ of 90° (Fig. 8(a)) has a helically trapped orbit and is lost as same with the 90 degrees ion for R =0.75 m in Fig. 7(a). An ion with χ of 100° (Fig. 8(b)) has a local mirror trapped orbit and is confined in one toroidal section. An ion with χ of 120° (Fig. 8(c)) has a passing orbit and is not interrupted by the first wall. Orbits launched from the position of R=0.90 m are presented in Fig. 9. An ion with χ of 95° (Fig. 9(a)) is lost immediately. An ion with χ of 100° (Fig. 9(b)) has a transition orbit between helically trapped orbits and passing orbits and is confined. An ion with χ of 120° (Fig. 9(c)) has a passing orbit and continues to circulate. Figure 10 shows orbits launched from the outside of device (R =1.10 m). Ions with χ of 90° and 110° (Fig. 10(a) and(b)) hit the first wall with short orbits. An ion with χ of 120° has a passing orbit circulating around the center of plasmas (Fig. 10(c)). From these figures, it is understood that the behavior and the region of confinement/loss of fast ions are determined by the real space and the velocity space of fast ions. The region of confinement/loss in R-χ space is called as the loss cone diagram and was investigated in detail on CHS by Sanuki *et al.* [35].

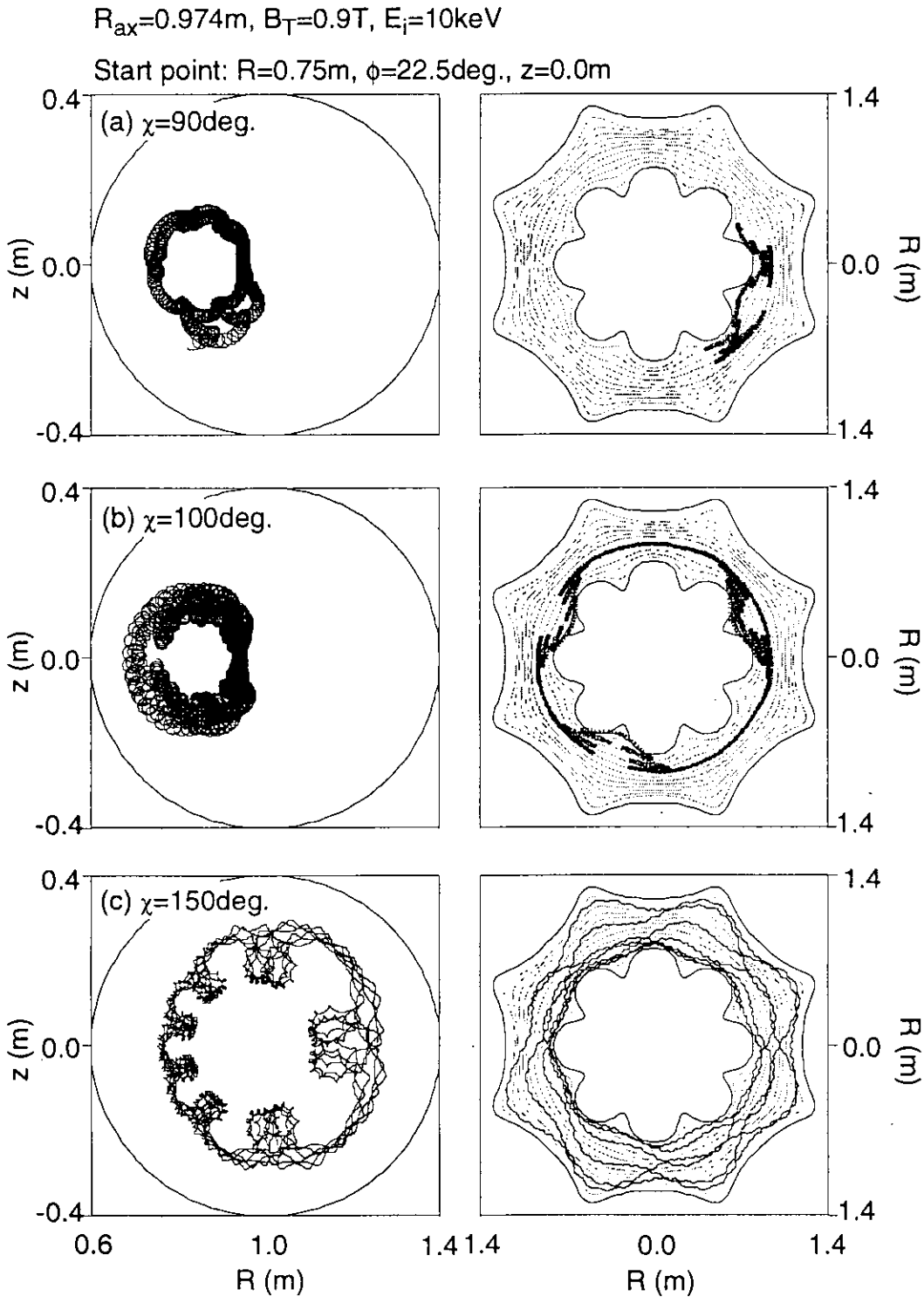

Fig. 7. Fast ion orbits in CHS (R=0.75 m, ϕ=22.5 deg., z=0.0 m).

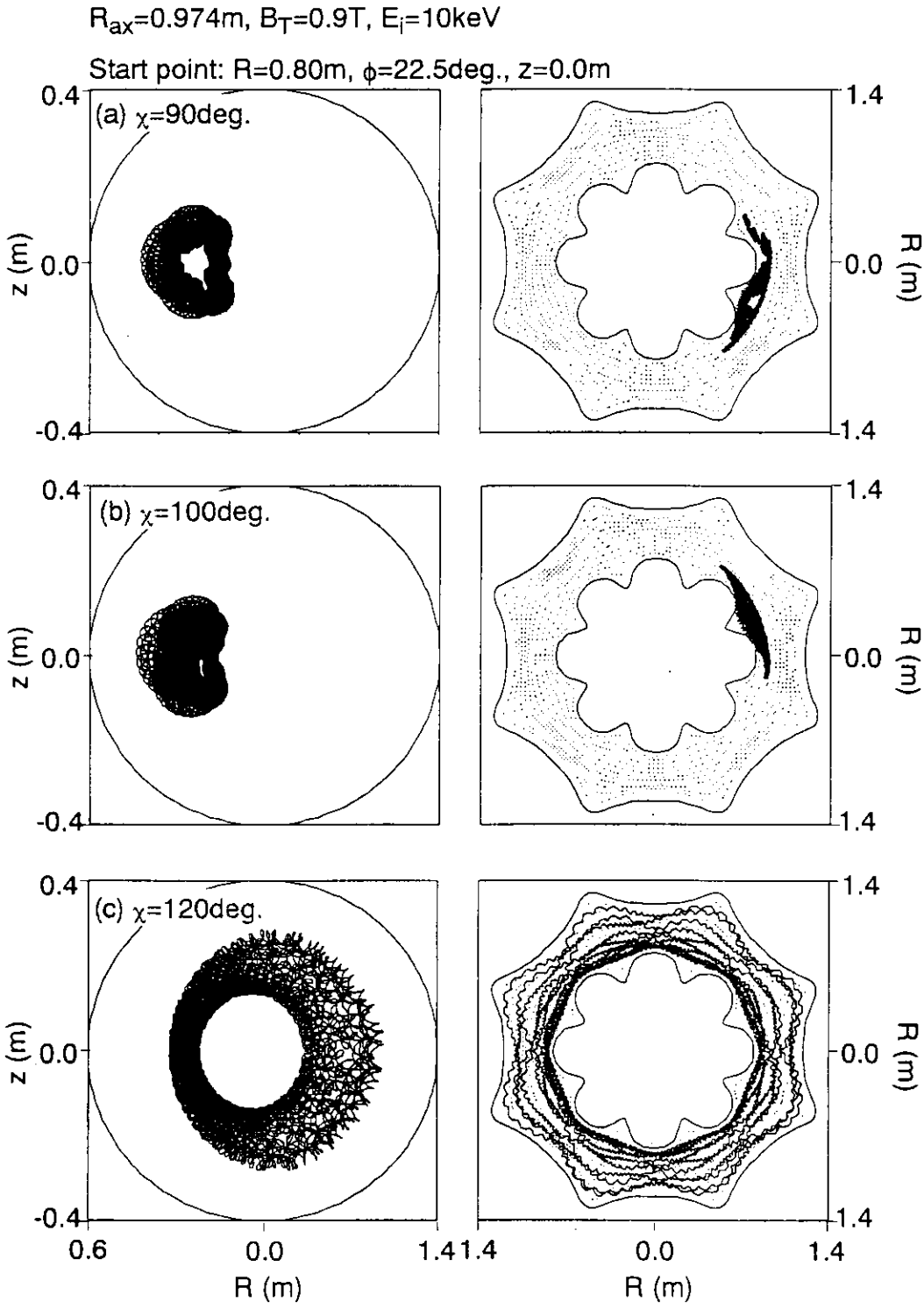

Fig. 8. Fast ion orbits in CHS (R=0.80 m, ϕ=22.5 deg., z=0.0 m).

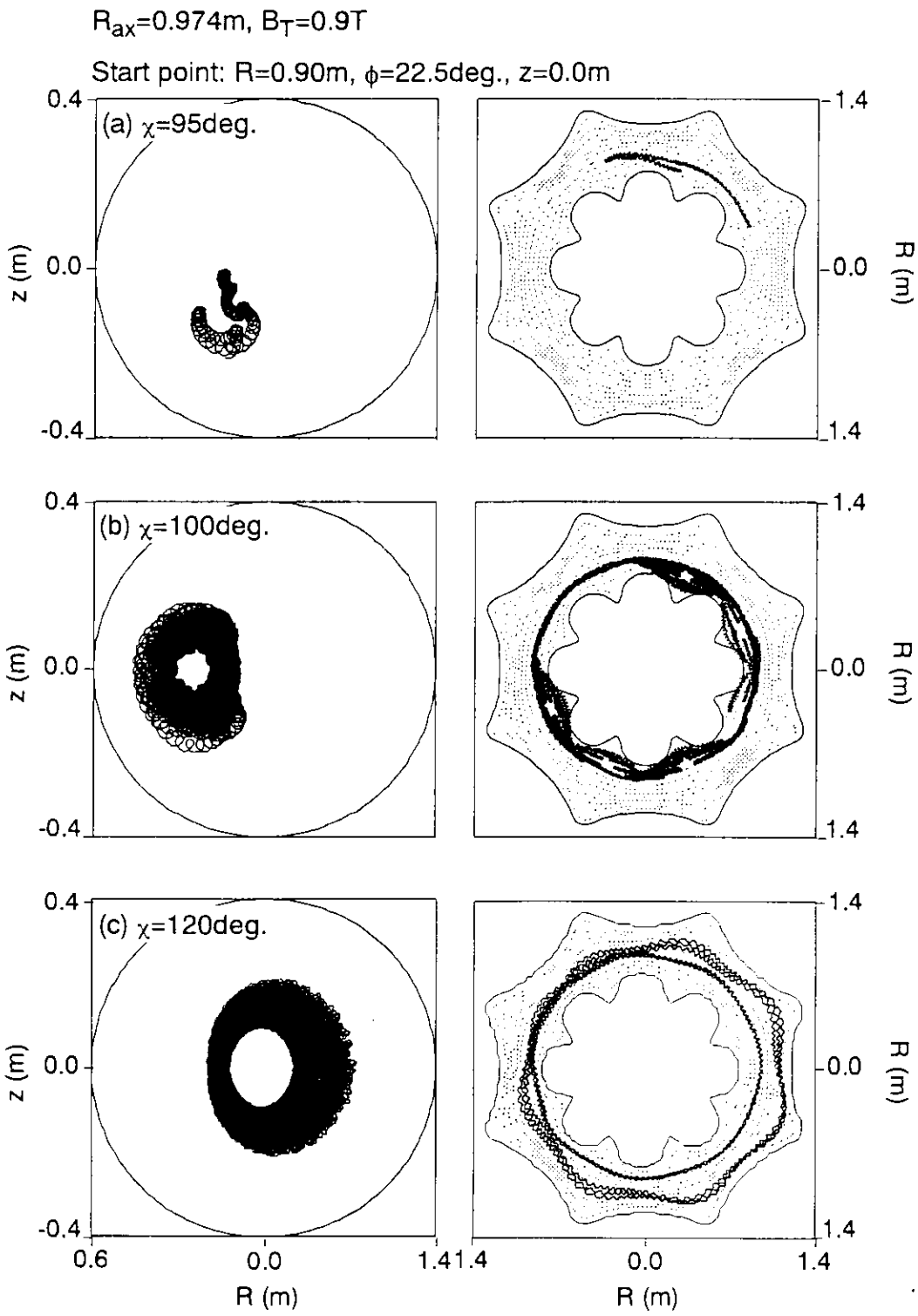

Fig. 9. Fast ion orbits in CHS (R=0.90 m, ϕ=22.5 deg., z=0.0 m).

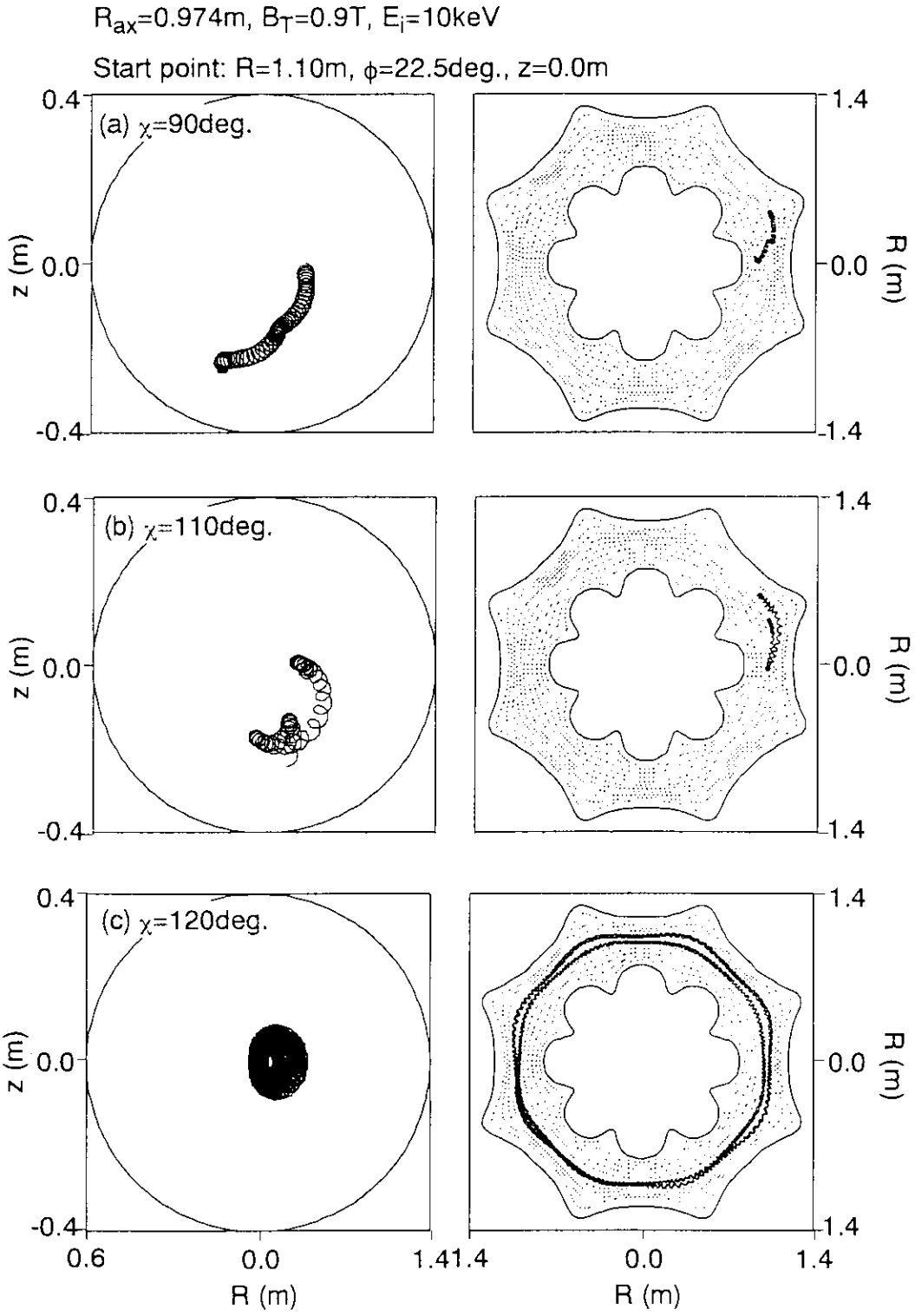

Fig. 10. Fast ion orbits in CHS (R=1.10 m, ϕ=22.5 deg., z=0.0 m).

Chapter 3

Experimental setup

3.1 Lost fast ion probe

3.1.1 Probe system and feature of this measurement

Figure 11 shows the schematic diagram of the lost-fast-ion probe [36]. The detector comprises a scintillator plate made from ZnS, fixed in a metal box with a pair of apertures on the side wall. Scintillator has advantages of good time resolution (~50 ns for ZnS), good spatial resolution (~10 μm grain size) and radiation resistance *etc.* for this measurement. The scintillator material with a thickness of 3~5 mg/cm^2, which is enough to stop 40 keV protons is smeared on a glass plate. The plate size had been 2.5 cm x 2.5 cm through February 1998 and was expanded to 3.2 cm x 3.2 cm to enhance the probe performance in March 1998. The probe has the feature that the positions on the scintillator plate struck by incident fast ions provide by information about the gyroradius and pitch angle of the ions. Therefore, the energy distribution and the pitch angle distribution of ions can be obtained by an analysis of the light pattern on the plate. The light is guided with a lens in the probe shaft to a beamsplitter. The beamsplitter divides the light into two paths. The light pattern as a 2D image is detected by a CCD camera (Hitachi Denshi, Ltd./KP-M1), coupled with an image intensifier (Hamamatsu/V2697HX). These images are recorded on video tape with a conventional video cassette recorder (Victor/HR-X7) with a time resolution of 33.3 ms. Recorded images are digitized by using a Macintosh computer equipped with a frame grabber board (Hamamatsu/IQ-V50). A nine-channel fiber array coupled to a

photomultiplier tube (PMT, Hamamatsu/H5784) is installed on the probe to detect light from a limited region on the scintillator for each channel separately. This multi-channel array was installed in January 1998 while a single fiber which covered whole the area on scintillator had been used until December 1997. A time resolution of 50 μs is determined by the frequency response of PMT, while the sampling speed of the CAMAC analogue to digital converter is 100 kHz. A fast measurement with good pitch angle resolution is favorable for the investigation of the fast phenomena, *e.g.* MHD-induced fast ion loss [37].

3.1.2 Detection method of gyroradius and pitch angle of escaping ions

Figure 12 shows schematic drawing of escaping ion measurements. There is a pair of apertures on the side wall of probe. The apertures consist of the front aperture (0.5 mm high x 2 mm wide) and the rear slit (0.5 mm high x 14.8 mm wide, spacing between apertures ; 8.6 mm). Fast ions with gyroradius of several cm can pass through the apertures and bulk ions with that of several mm are interrupted to enter by the apertures. Here, the gyroradius ρ_i is given by $\rho_i = (2m_iE_i)^{0.5}/q_iB$, where m_i, q_i and B are mass, charge of an ion and magnetic field strength at the aperture position, respectively. Ions with larger ρ_i (higher energy) reach the point on scintillator far from apertures and those with smaller ρ_i (lower energy) hit the point near apertures. Struck positions depend on not only the energy of ions but also the incident angle of ions to apertures (or magnetic field line at the aperture position); pitch angle χ. Therefore the scintillation light pattern has the information on the χ–ρ_i profile of detected escaping fast ions.

3.1.3 Aperture direction for co- and counter-going ion measurements

The probe was inserted from the top of the device vertically as shown in Fig. 13, because the direction of ∇B drift of ions is upward in the standard operational condition of CHS. The center of the probe shaft is fixed at a major radius R=1.2 m. The top of the probe is placed at the position by 2 cm away from LCMS for R_{ax}=0.995m,

or of 7 cm for R_{ax}=0.921m.

As mentioned in section 3.1.2, the range of χ of detected ions is decided by the aperture direction. Figure 14 shows the aperture direction for co- and counter (ctr.) -going ion measurements. Parallel velocities of co-injected beam ions are opposite to the direction of magnetic fields in CHS. It is defined in this thesis that co-going ions have χ larger than 90° and ctr.-going ions have one smaller than 90°. In the case of the aperture angle of +45° to R direction, co-going ions which are in the range of χ from 100° to 145°can be detected. The ninety degrees rotation of the probe itself in the cw direction (aperture angle of -45°) makes it possible to detect ctr-going ions which are in the range of χ from 40° to 90°. In this study the aperture angle was changed from +45° to -45° in August 1998 to investigate co- and ctr. -going ion loss, respectively.

3.1.4 Faraday cup structure for direct measurements of escaping ion currents

Absolute flux of escaping ions into the probe is important information for the estimation of fast ion loss rate. For a lost-fast-ion probe of the TFTR tokamak, which is a prototype of the probe on CHS, the calibration were made with the amount of scintillation light produced by alpha particle beams from an accelerator [38]. The probe on CHS has a function that the total absolute flux of ions incident on the scintillator can be measured as an ion current [39]. Figure 15(a) shows the schematic diagram of Faraday cup structure for direct measurements of escaping ion currents. The scintillator plate consists of three layers, a smeared scintillator, an aluminum layer of vapor deposition and a glass substrate. The edge of the scintillator plate is covered with a mica film, so that the scintillator on the Al-layer is isolated electricaly from the probe body. The ion current signal of incident protons is converted to the voltage signal with a resister of 470 kΩ or 100 kΩ and is transferred to CAMAC through an amplifier with an amplification factor of 100. Typical current signal measured by this system is shown in Fig. 15(b). No current signal was observed except during NBI. The time behavior of current signal is similar to that of fast ion loss signal (PMT output)

shown in section 4.1.

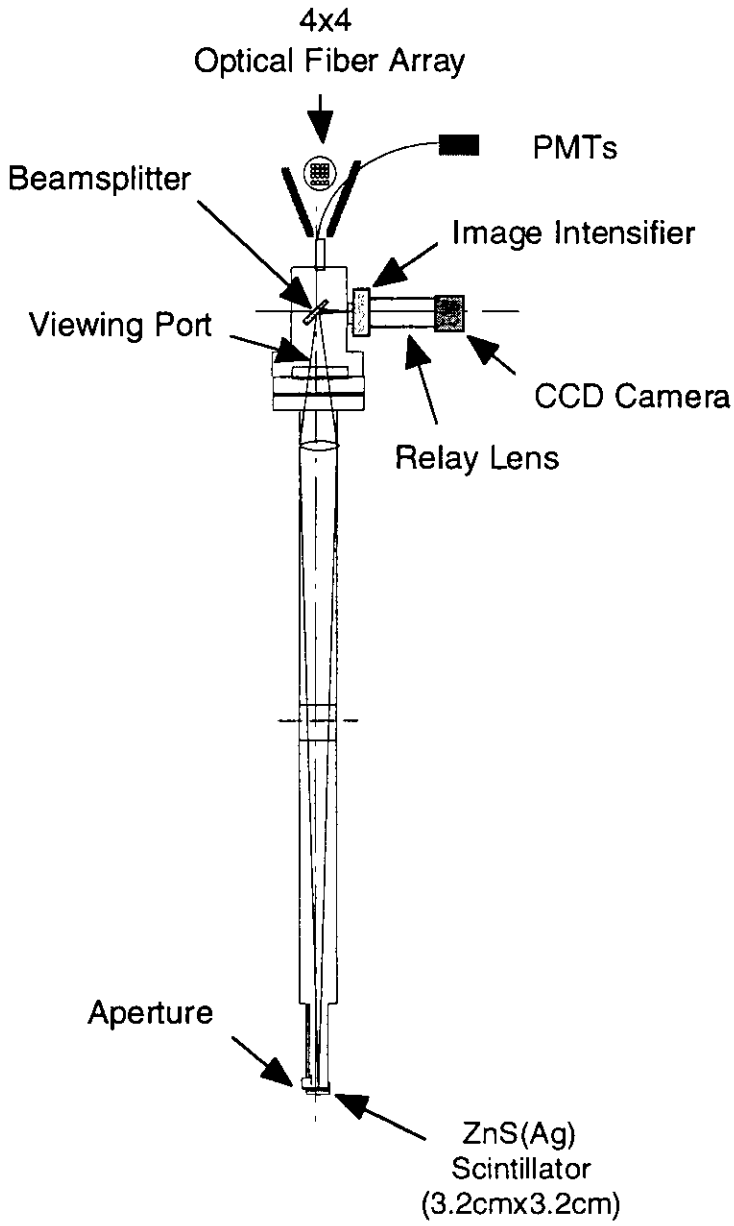

Fig. 11. Schematic diagram of the scintillator-type lost-fast-ion probe. The light emitted from the scintillator is divided by the beamsplitter to two detection paths and is detected by the PMT array and the CCD camera.

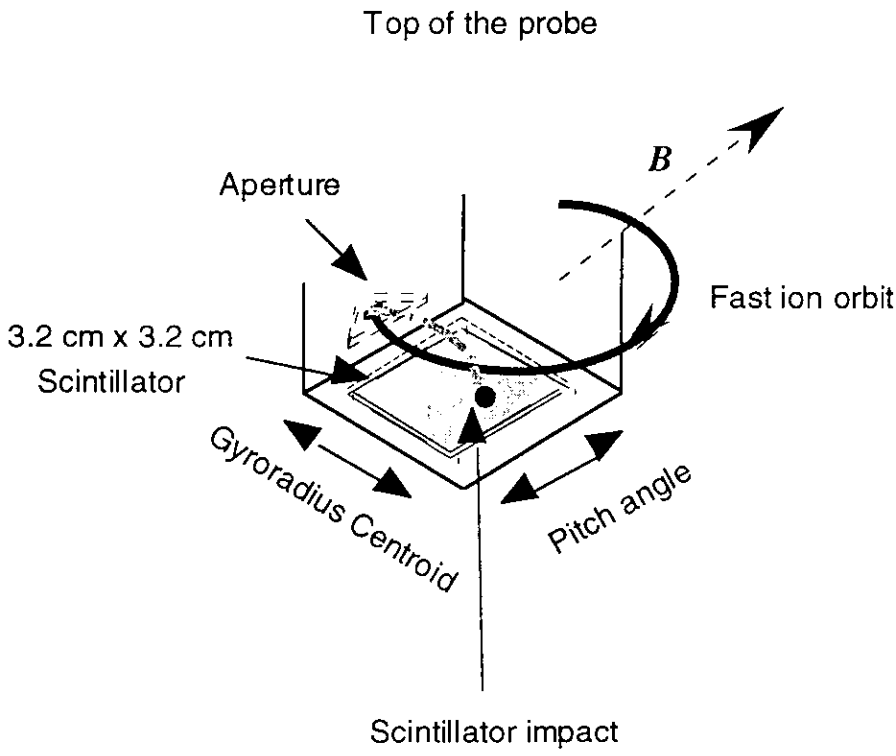

Gyroradius Centroid ρ

$$\rho_i \equiv \frac{\sqrt{2mE_i}}{qB}$$

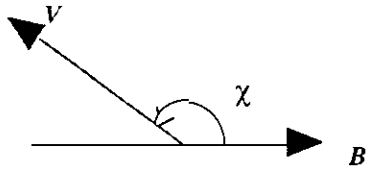

Pitch Angle χ

$$\chi \equiv \cos^{-1}\left(\frac{v_{\parallel}}{v}\right)$$

Fig. 12. Schematic diagram of escaping ion measurements.

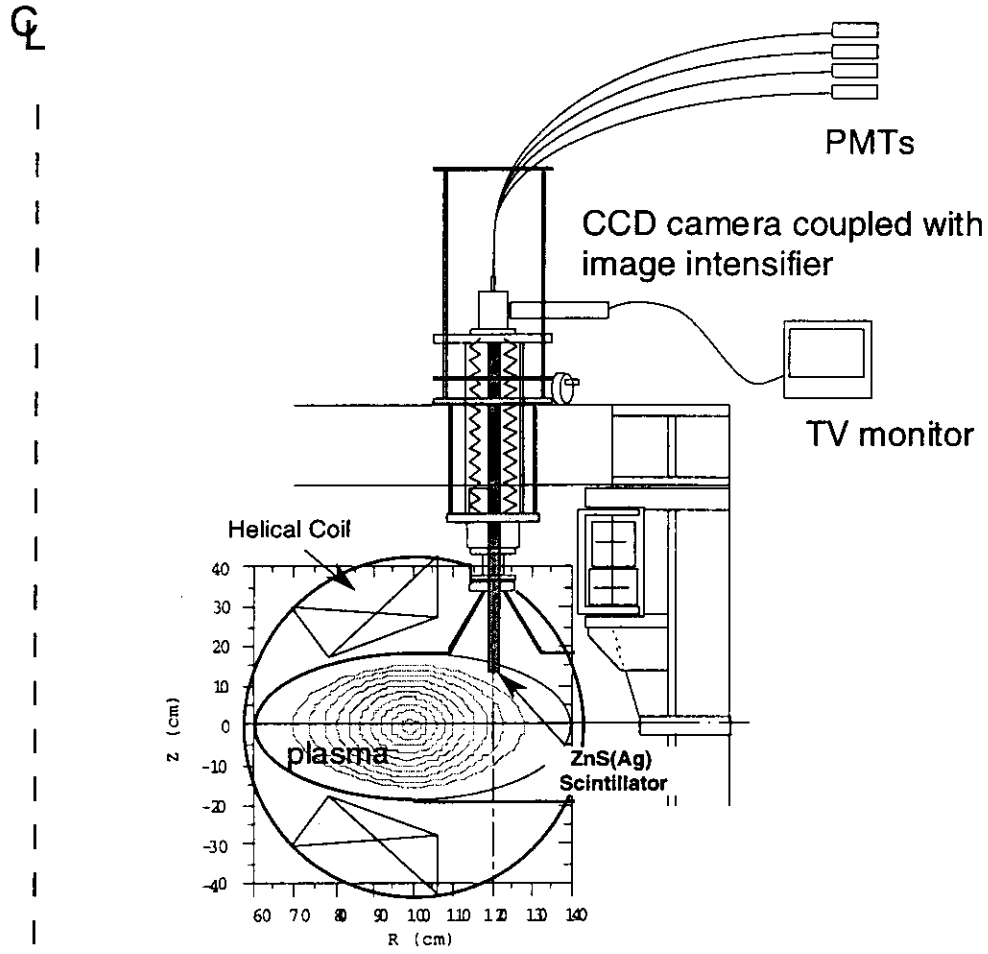

Fig. 13. Vertically inserted lost-fast-ion probe on CHS.

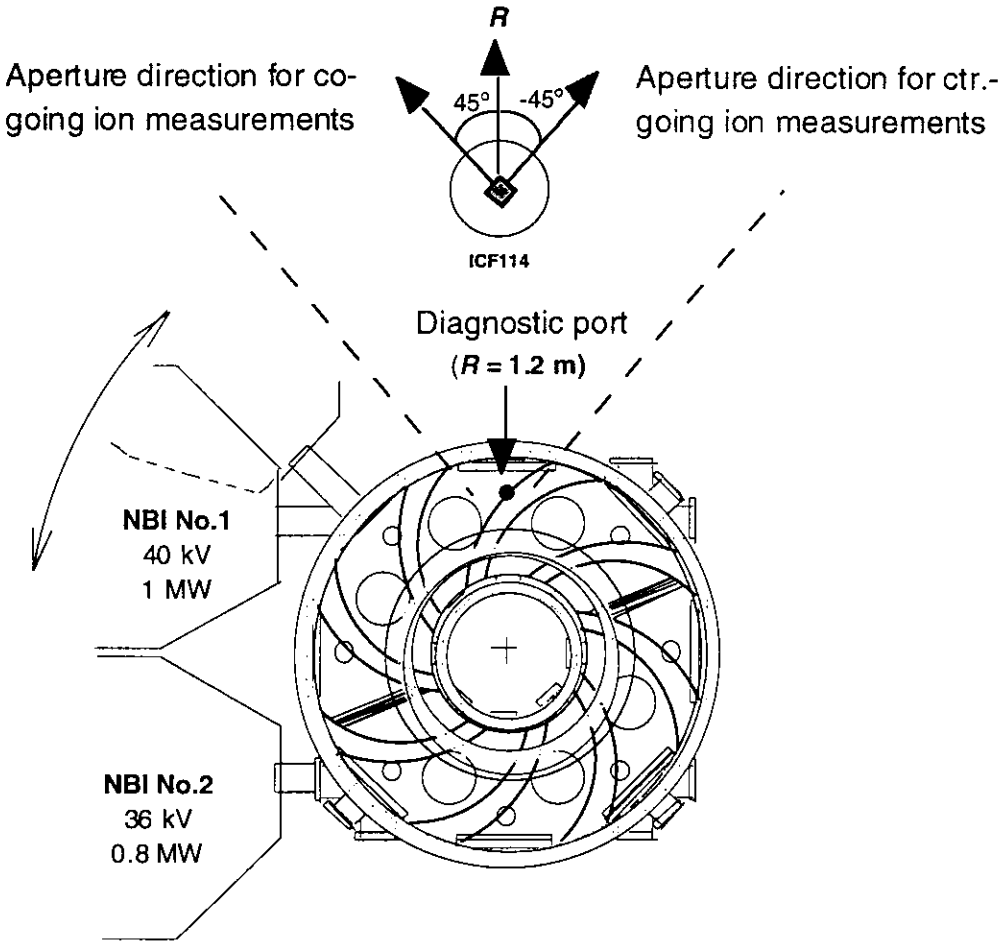

Fig. 14. Lost-fast-ion probe on CHS (top view). Aperture directions for co- and counter -going ion measurements are shown.

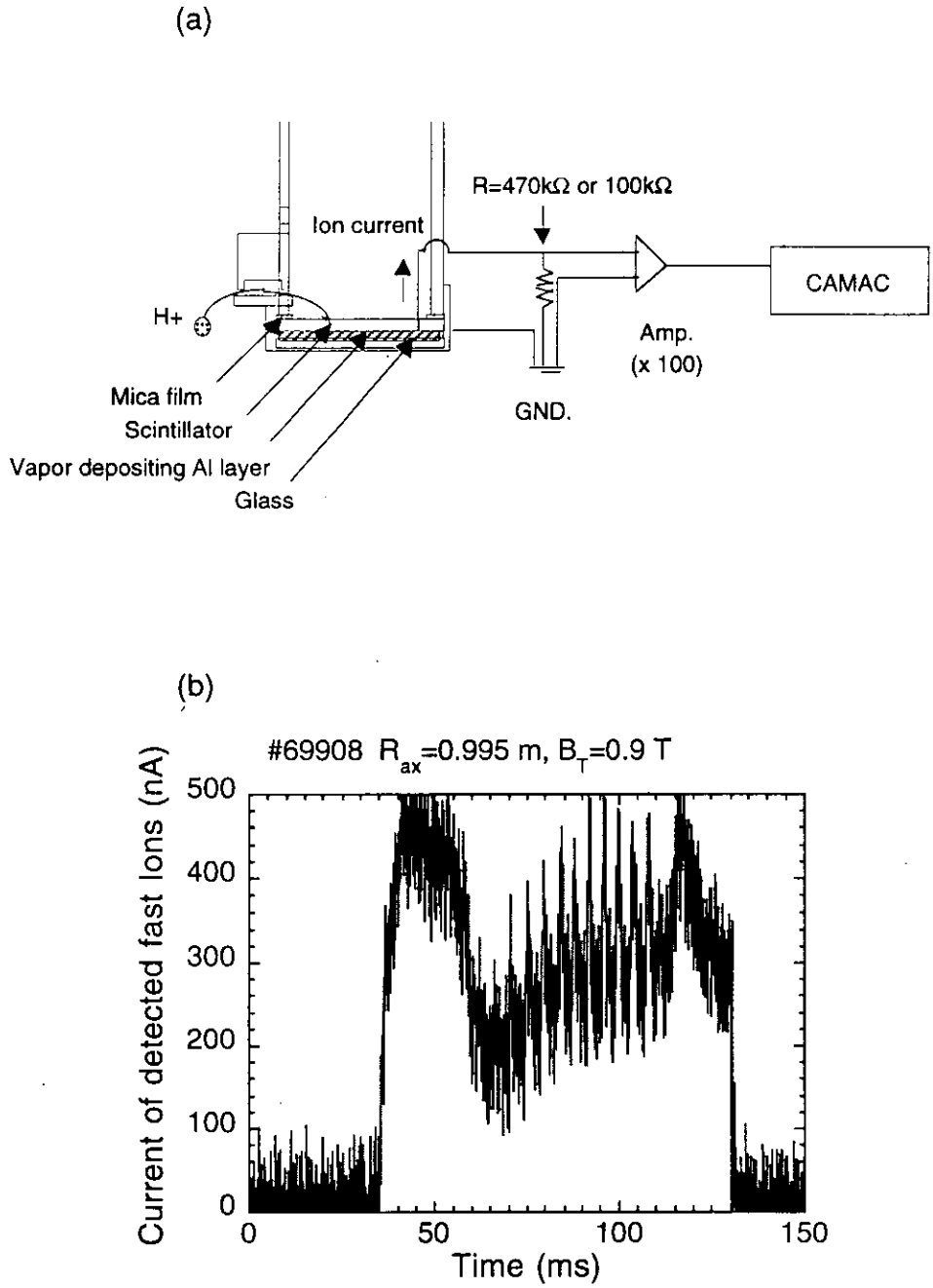

Fig. 15. Schematic diagram of Faraday cup structure for direct measurements of escaping ion currents, (a) and typical signal of escaping ion currents, (b).

3.2 Calibration of instruments

3.2.1 Gain characteristic of PMTs

In the beginning of measurements, calibration works for the gain characteristic of instruments were made to compare the signal intensity among each of plasma discharges measured with different gain of these instruments or each of PMTs. On this probe sixteen PMTs were used. The PMTs with a internal amplifier have the frequency response of 20 kHz and the maximum sensitivity for the light wavelength in the range of 300~500 nm which covers the characteristic wavelength of lights emitted from ZnS(Ag), 450 nm. Gain characteristics for these PMTs were obtained by using a simple circuit as shown in Fig. 14(a). A light emitting device (LED) whose luminance is controlled was used as a variable light source but steady. Under the steady luminance condition, output voltage values, V_{out} of a PMT were recorded with changing the externally applied bias, V_c for the PMT gain control and the results are plotted in Fig. 14(b). The characteristic curves with almost equal powers were obtained for two kinds of LED luminance, 61 and 2.0 μcd. This calibration work were done for each of sixteen PMTs.

3.2.2 CCD camera view

Position of light pattern on the scintillator plate has the important information for this measurement as mentioned in section 3.1.2. Images from the CCD camera are recorded on video tape as presented in Fig. 17. The light pattern viewed by a CCD camera can also be seen on a TV monitor. Calibration to identify the position of the scintillator edge on the monitor and the video frame is necessary because of determination of the position of light pattern on the scintillator. The size of area on scintillator which can be seen by the CCD camera, 27.5 mm x 29 mm, is optically shrunk by a factor of 0.275 with a relay lens installed in the middle of probe shaft to

adjust to the size of image region of the CCD camera (8.8mm x 6.6 mm, 2/3 inch size). Therefore the tiny difference in position of installed instruments becomes the large difference in position of images in the camera view and this causes the ambiguity of the light pattern position, when the probe is removed from CHS for calibration. To avoid this problem the in-situ calibration is necessary. For this purpose a small lamp was installed inside the probe shaft to illuminate the scintillator [39]. Figure 18(a) shows the schematic view of the lamp inside the probe shaft. Illuminated scintillator in a video frame is shown in Fig. 18(b). The intense light spot in the figure is just under the lamp. The scintillator edge is seen as dim lights in the drawn square. By means of this in-situ calibration method the position of scintillator edge is known accurately.

3.2.3 PMT array view

The light pattern on the scintillator is viewed by the optical fiber array connected with the PMT array to measure time evolutions of escaping fast ion flux in the limited range of χ and ρ_i, simultaneously. Positions of each view of PMTs on the scintillator have to be known. The in-situ calibration is necessary to determine the positions because of the problem as mentioned in section 3.2.2. The in-situ calibration work to determine the position of each fiber view was carried out using a laser light transmitted in the reverse direction from the output of the optical fiber onto the scintillator as shown in Fig. 19(a). Figure 19(b) shows the illuminated laser light spot on the scintillator viewed by the CCD camera. The black circle on the light spot presents the optical fiber size (ϕ1.5 mm) on the scintillator. The size of light spot agrees well with that of the circle. The work was done for each of PMTs and the position of PMT array view was determined accurately.

3.2.4 Gain characteristic of image intensifier

An image intensifier is installed in front of the CCD camera because of the weakness of the intensity of lights emitted from the scintillator. For the image

intensifier, a calibration work to obtain the gain characteristic was made. This work was done after the inspection of probe signal because lights emitted from the scintillator due to escaping fast ions were used as a light source of steady intensity which was monitored by PMT under the constant plasma conditions. Figure 20 shows the gain curve of the image intensifier. Image intensities which were taken numerically on digitized images were recorded with changing the image intensifier gain. Comparison among signal intensities of images measured with different gain can be made using this gain curve.

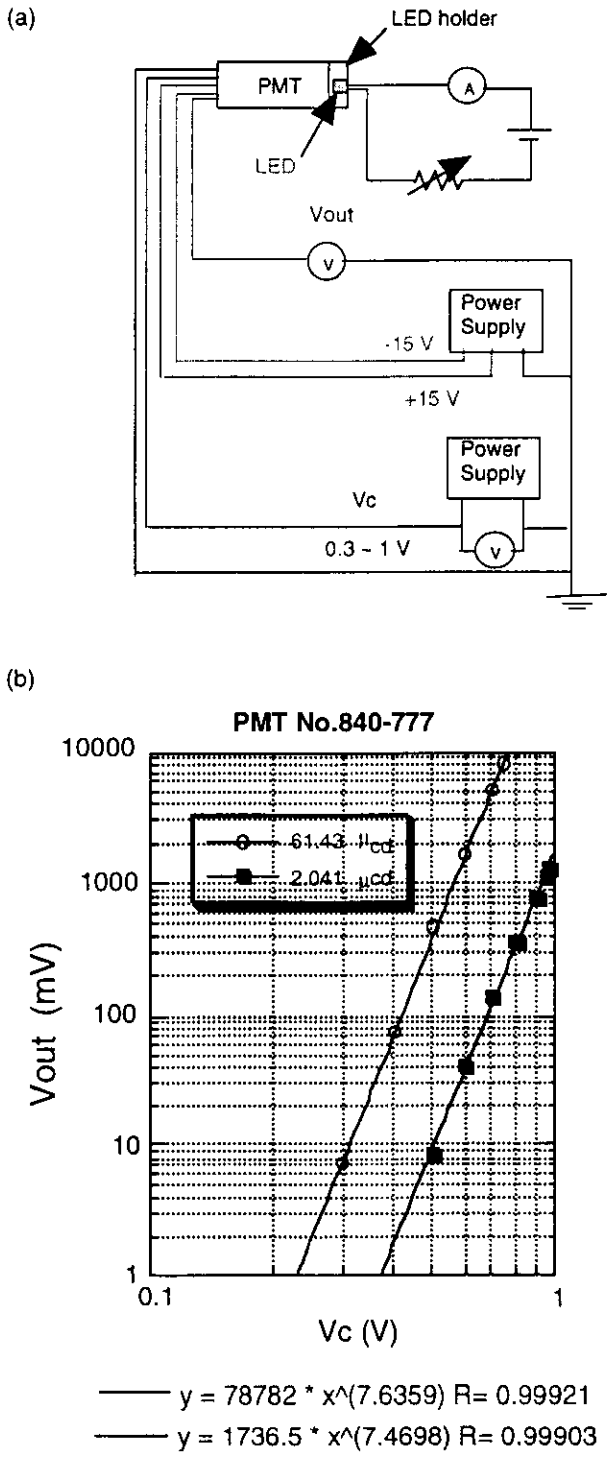

Fig.16. Schematic diagram of gain calibration system for PMTs, (a) and the gain characteristic of a PMT, (b).

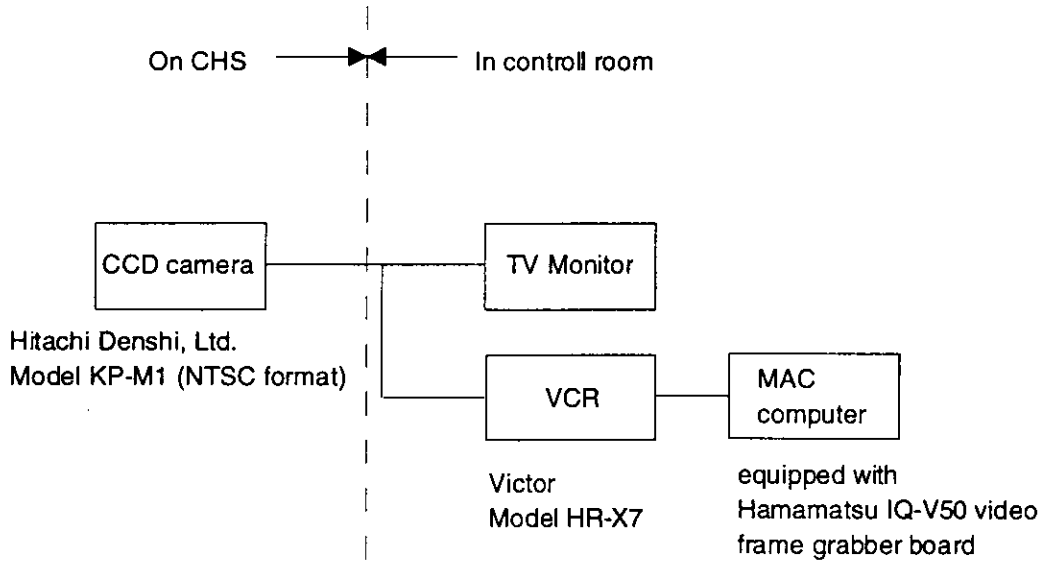

Fig. 17. Data acquisition system for CCD camera images.

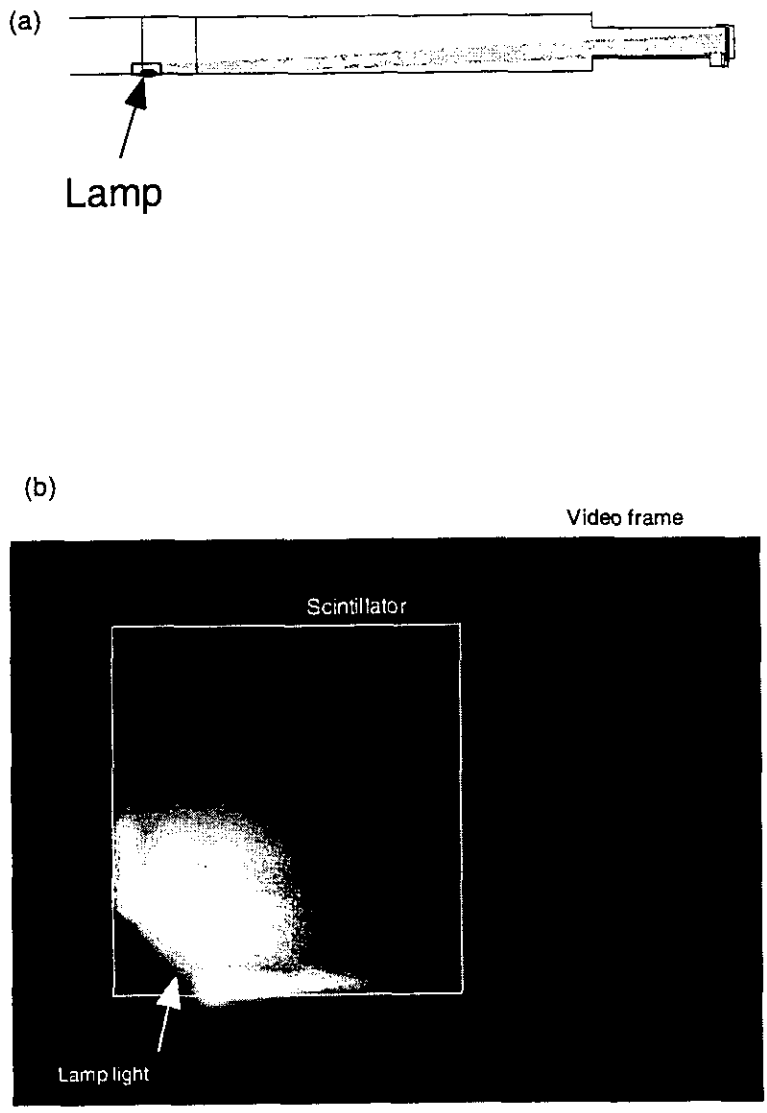

Fig. 18. Schematic diagram of lamp mounting configuration inside the probe shaft for position calibration of CCD camera views, (a) and position of the scintillator edge in the video frame, (b).

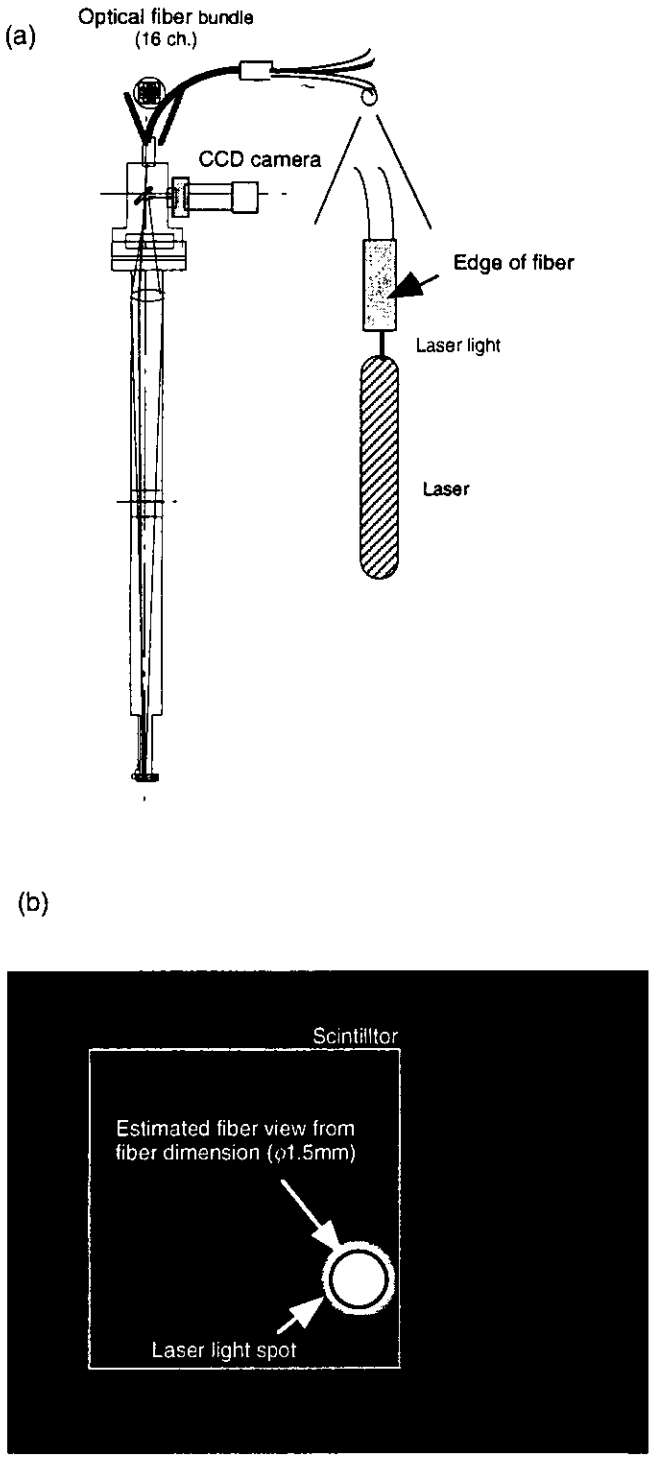

Fig. 19. Position calibration of PMT array view with a laser light. (b)Position of PMT in the video frame.

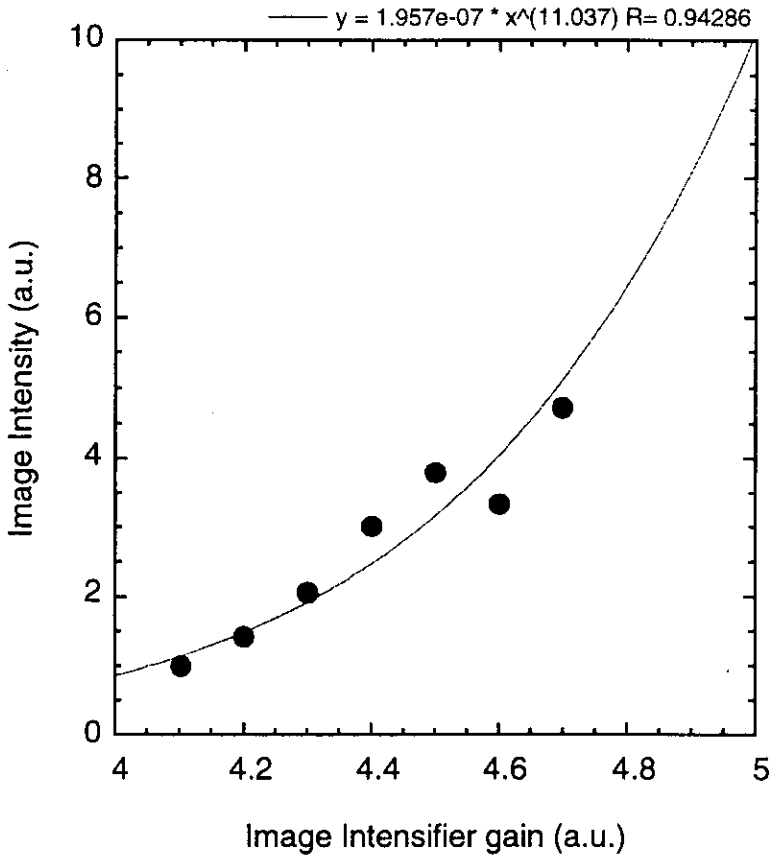

Fig. 20. Gain characteristic of the image intensifier.

3.3 Gyroradius and pitch angle calculation

3.3.1 Gyroradius and pitch angle grid on scintillator

Position on the scintillator has the information on χ and ρ_i of detected escaping fast ions. The "grid" of χ and ρ_i on the scintillator is calculated by using the detector simulation code [10]. In the code, ions are launched from the front aperture position with changing χ and ρ_i as shown in Fig. 21. The direction of magnetic field at the aperture position is determined by the magnetic configuration of CHS. The grid can be made by linking the peak position of χ and ρ_i distribution composed by points struck by launched ions. The details of χ and ρ_i distribution are described below. Calculated grids together with the PMT array view are shown in Figs. 22(a) and (b) for the measurements of co-going ions and ctr- going ions, respectively. Each circle on the scintillator shown in the figures presents the each of PMT views in the range of limited χ and ρ_i.

3.3.2 Estimation of energy resolution

This probe has a poor energy resolution due to the finite aperture size (the front aperture is 0.5 mm high x 2.0 mm wide, the rear one is 0.5 mm high x 14.8 mm wide and the spacing between apertures is 8.6 mm). When mono energy ions are launched from the aperture, they impinge upon the scintillator depending on the center position of their gyro motions. Figure 23(a) shows the schematic view of the influence of the difference of the guiding center positions on the difference of the struck positions. This is due to the finite aperture size and is the cause of poor energy resolution of this probe. The energy resolution was estimated using a detector simulation code for R_{ax}=0.995 m and B_T=0.9 T as shown in Fig. 23(b). When 40 keV ions, for example, are launched from the aperture, they are dispersed on the scintillator depending on the center position of their gyro motions, in the distribution with gyroradius centroid of 4.1

cm and with FWHM of 3.0 cm in the simulation. The shadowed regions in Fig. 23(b) show the regions covered by the field of views of channels 6 and 7 of the PMT array (Fig. 22(a)). The region of ch.7 involves distribution of ions with E_i from 5 to 20 keV and that of ch.6 involves those with E_i from 20 to 40 keV. Resolution of χ, $\pm 2.0°$ is determined by the geometrical configuration of apertures.

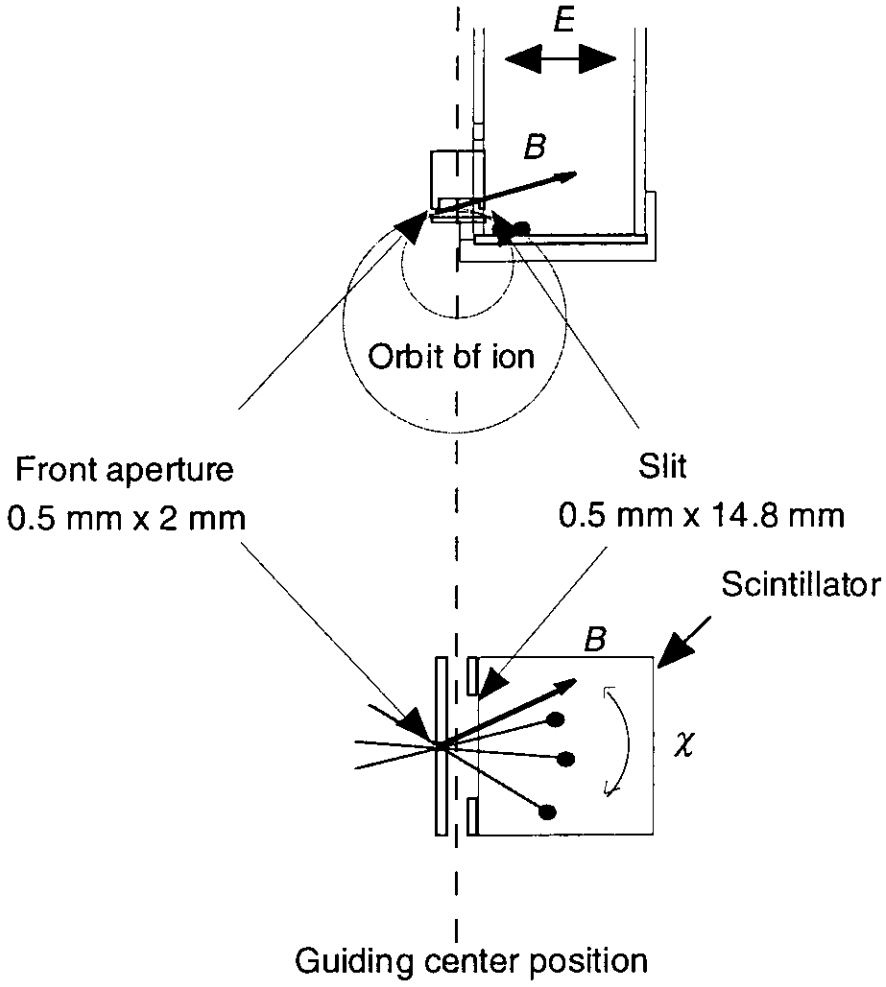

Fig. 21. Calculation of the χ–ρ_i grid on the scintillator.

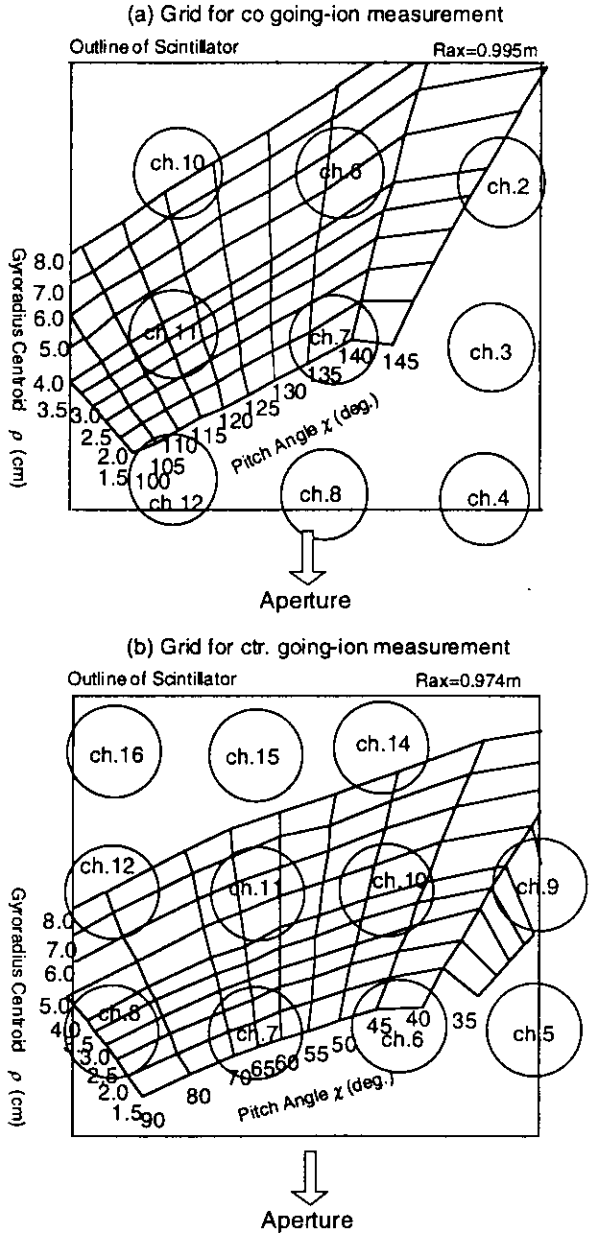

Fig. 22. Views of the PMT array with the grid on the scintillator. Circles in the figure show each view of the PMT array. (a) Grid for measurements of co-going ions in the range of the pitch angle from 100° to 145°. (b) Grid for measurements of ctr-going ions in the range of the pitch angle from 35° to 90°. The probe itself was rotated by 90° in the clockwise direction viewing from above to detect ctr-going ions.

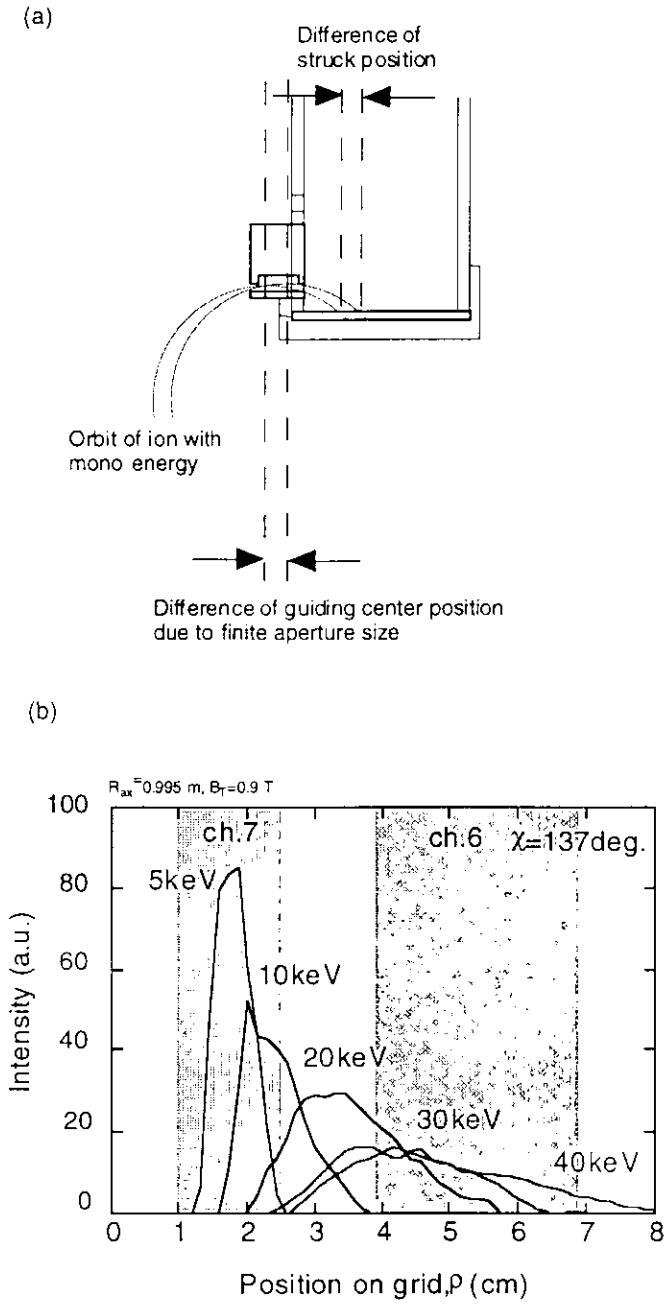

Fig. 23. Estimation of energy resolution, (a) and the cause of ambiguity in energy, (b).

3.4 Magnetic probe array

Magnetic probes are powerful diagnostics for the study of MHD instabilities to measure magnetic fluctuations and are extensively used in magnetic confinement devices. In CHS, the toroidal and poloidal magnetic probe arrays to analyze MHD instabilities are installed as shown in Fig. 24 [30, 40]. There are five probes on the N-ports and four probes on the G-ports in toroidal direction. The poloidal magnetic probe array has sixteen probes and is installed in one toroidal location presented in Fig. 24. These probes have a frequency response of up to ~200 kHz. By using these probe array, mode numbers, m and n, propagating direction and velocity of magnetic fluctuations are derived by an analysis of phase difference among signals measured at different locations. Characteristics in frequency of magnetic fluctuations are investigated from power spectrum obtained with FFT analysis. The poloidal and toroidal arrays are used effectively to identify the poloidal/toroidal modes of MHD, for some typical discharges of this study. Some of these magnetic probes are always measuring the magnetic fluctuations through the present work.

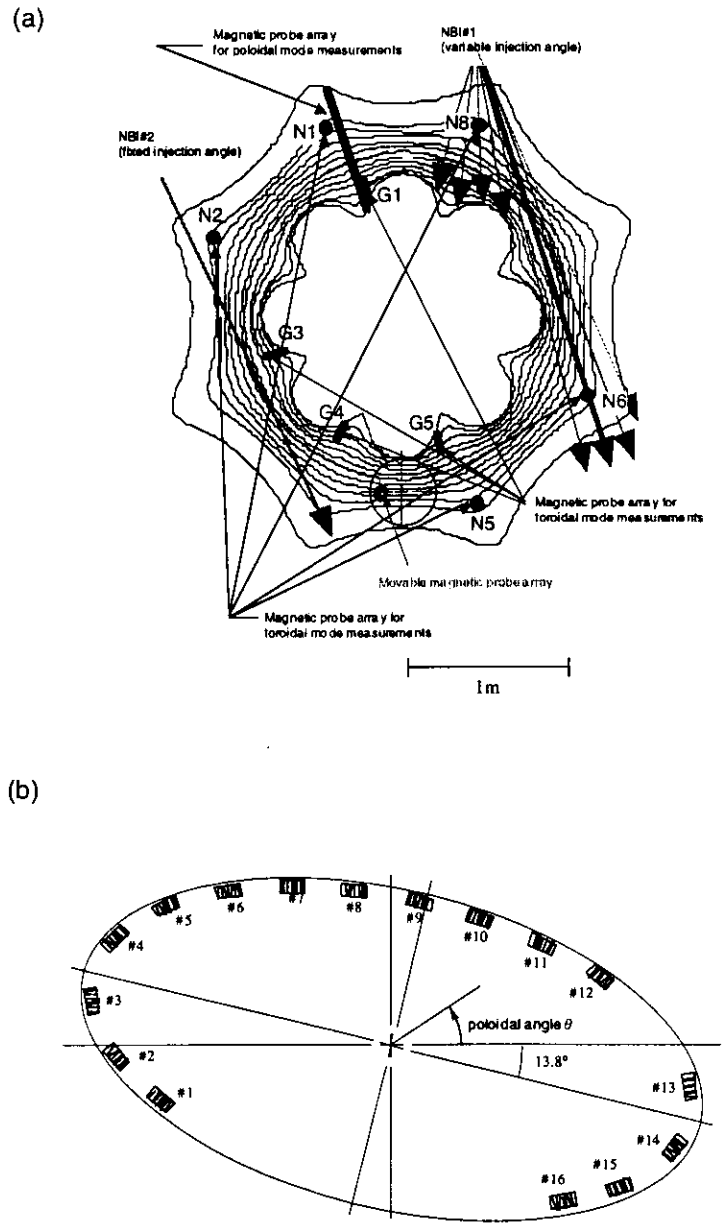

Fig. 24. Magnetic probe array for toroidal (a) and poloidal (b) mode measurements [30].

Chapter 4

Measurements

4.1 Inspection of fast ion loss signal

The measurement was first applied to NB heated plasmas in CHS in March 1997. At the time, the single channel optical fiber coupled to a PMT was installed on the probe as mentioned in section 3.1.1. First of all, it was inspected that the probe signal did not arise from X-rays due to runaway electrons, plasma lights and other noises, but from escaping beam ions. As a simple method to inspect the signal, the ∇B drift direction was changed from upward, which was toward the probe, to downward by changing direction of B_T from counter clockwise direction (CCW) to clockwise direction (CW) as seen from top of the device. Figure 25 shows the probe signals (single channel PMT) derived in discharges with B_T of CCW (#61819) and CW (#61826). Magnetic field configuration was as follows; R_{ax} of 0.974 m and B_T of 0.9 T. Plasmas were initiated by ECH and heated by NBI. In the case of CCW, a signal was observed clearly just during NBI, while no signal was seen in the case of CW. Moreover, no other noise arising from X-rays or H_α lights was seen for both discharges when NBI was off.

Next, signal characteristics depending on plasma parameters were investigated. Measurements of signals were made with changing B_T because position of light pattern due to escaping fast ions on the scintillator is predicted to move depending on magnetic field strength. Figure 26 shows variation of position of light pattern detected in plasmas with R_{ax} = 0.949 m with changing B_T. It is seen that light patterns moved to the position predicted from the magnetic field strength at the probe position with

changes B_T. Dependence of signal intensity measured with PMT on B_T is presented in Fig. 27. The signal intensity decreased drastically with increasing B_T. This is explained by using the orbit calculation as follows; passing boundary ions which make the most intense light pattern can not reach the probe for the case of B_T greater than 1.2 T. Dependence of signal intensity on R_{ax} was investigated for discharges with B_T of 0.9 T and is presented in Fig. 28. Signal intensity increased drastically as R_{ax} moved to outward (plasmas come close to the probe). An analysis giving an explanation for the characteristic is made in Ref. 46. Increase of signal intensity with n_e was observed as shown in Fig. 29. Increase of deposition fraction of NB computed with the HFREYA code, R_{dep} would be a reason of increased loss signals.

From these results, it is concluded that probe signals are due to detected escaping fast ions, except for other noises.

Fast ions having large deviation from magnetic surfaces near LCMS suffer from interruptions by in-vessel components. Therefore, influence of in-vessel components on fast ion signals was investigated. In the vacuum vessel of CHS, there are many components, for example those for diagnostics, including the lost-fast-ion probe itself. Among these components, a radially movable IBW antenna (approximately 150 mm x 500 mm in size) used as a limiter located close to LCMS has large influence on interruptions of fast ion orbits. Fast ion signals were measured with changing radial position of the antenna, shot by shot. Magnetic field configuration with R_{ax} = 0.949 m and B_T=0.9 T was employed. Figures 30(a) and (b) show dependence of the pitch angle distribution and the gyroradius distribution of detected ions on antenna positions, respectively. These distributions are derived from detected light patterns on the χ-ρ_i grid (Fig. 22). The intensities plotted in Fig. 30(a) for each of χ are the integrated values over ρ_i on constant χ and those in Fig. 30(b) for each of ρ_i are the integrated values over χ on constant ρ_i. Strong influence on these profiles was observed, especially for fast ions with χ of around 135° and ρ_i of around 4 cm. These ions are classified as "passing boundary ions" which are on the boundary between passing ions and loss cone, and have large deviation from magnetic surfaces. Signal intensity

decreased with inserting the antenna which intersects fast ion orbits. From this investigation the distance of 6.0 cm has less influence on experiments. But the antenna has a role as a limiter to suppress X-ray emission due to runaway electrons and is located to observe a regulation on radiation protection. Therefore fast ion measurements in this study were made with fixed antenna positions for each of R_{ax}.

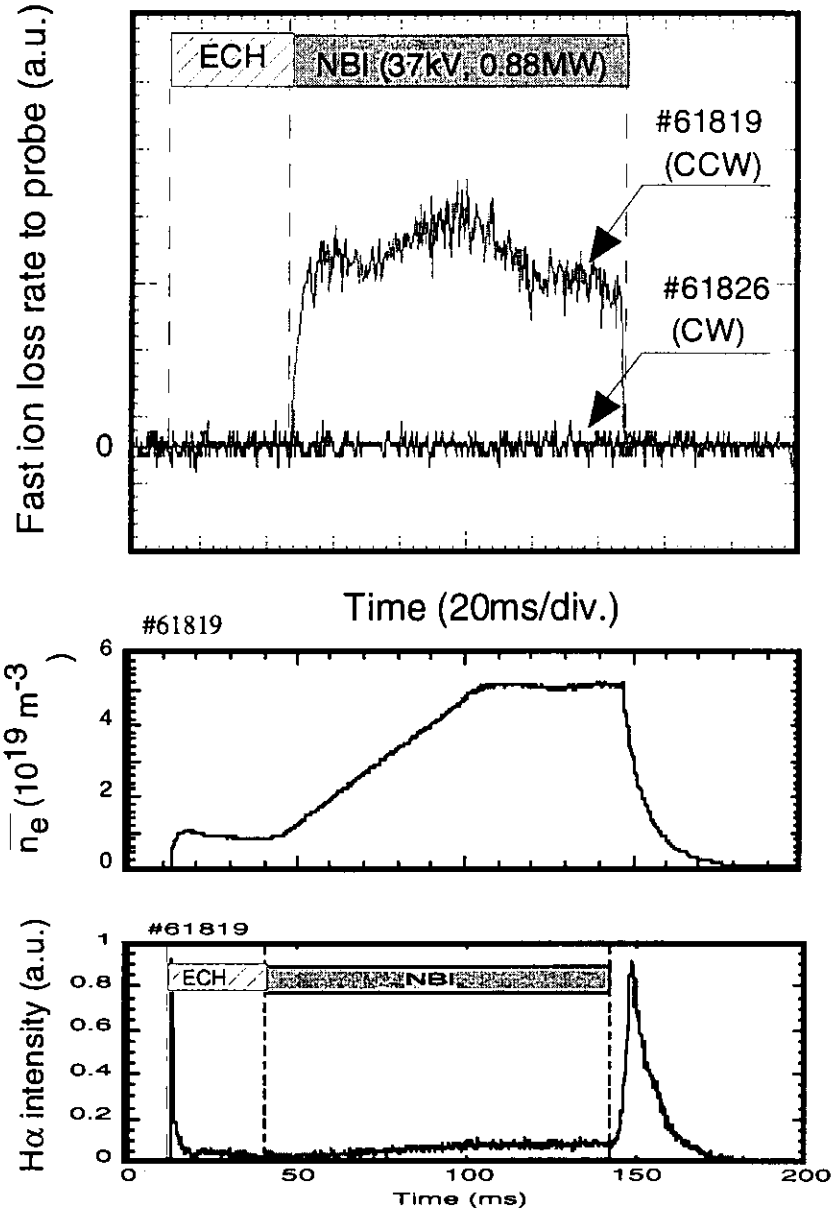

Fig. 25. Lost-fast-ion probe signal measured in discharges with BT of CCW (#61819) and CW (#61826). In the case of CCW, a signal was observed clearly just during NBI, while no signal was seen in the case of CW. No other noise arising from X-rays or Hα lights was seen for both discharges.

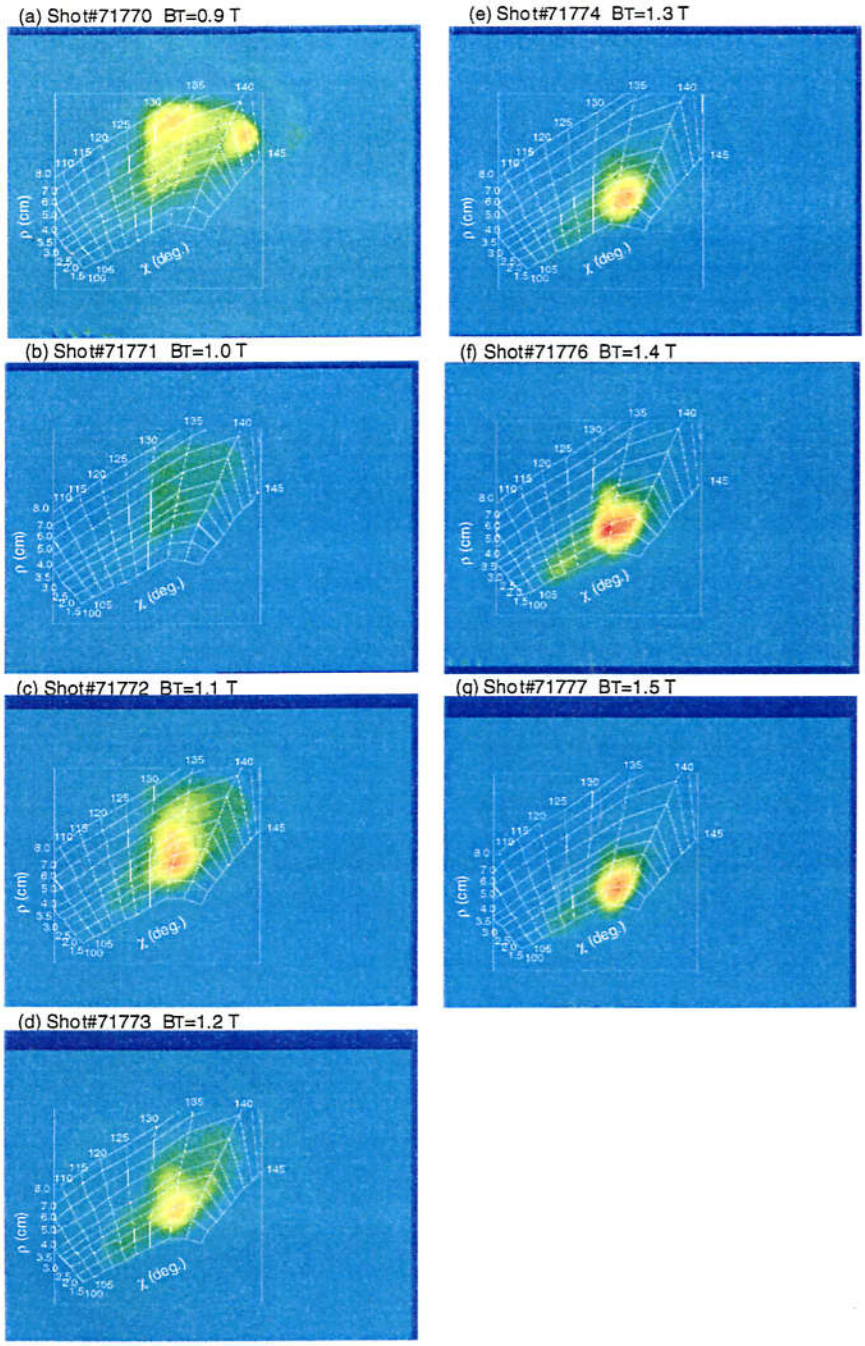

Fig. 26. Variation of position of light pattern with changing of B_T. It is seen that light patterns moved to the position predicted from the magnetic field strength at the probe position with changes of B_T.

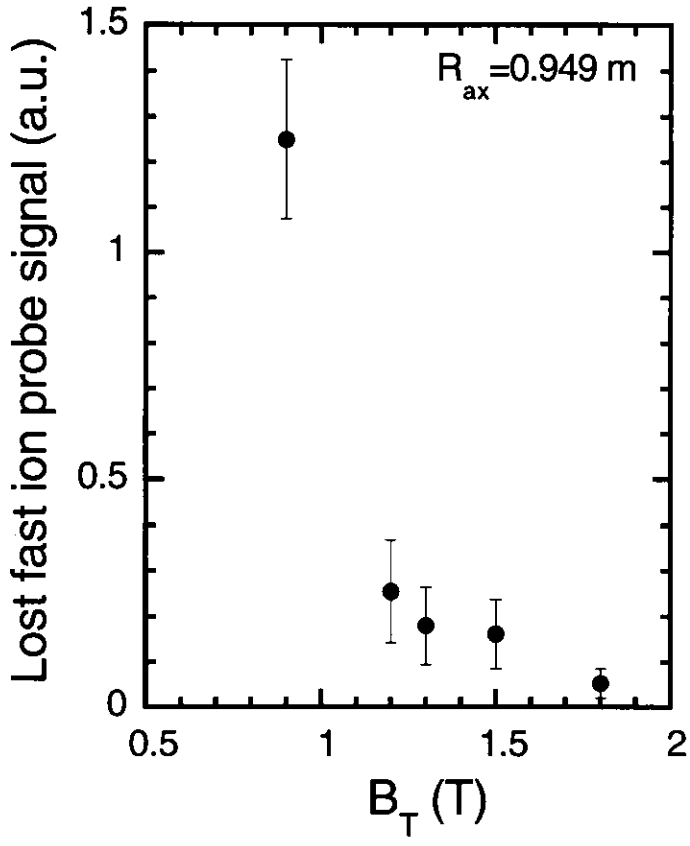

Fig. 27. Dependence of fast ion loss probe signal intensity measured with single channel PMT on B_T.

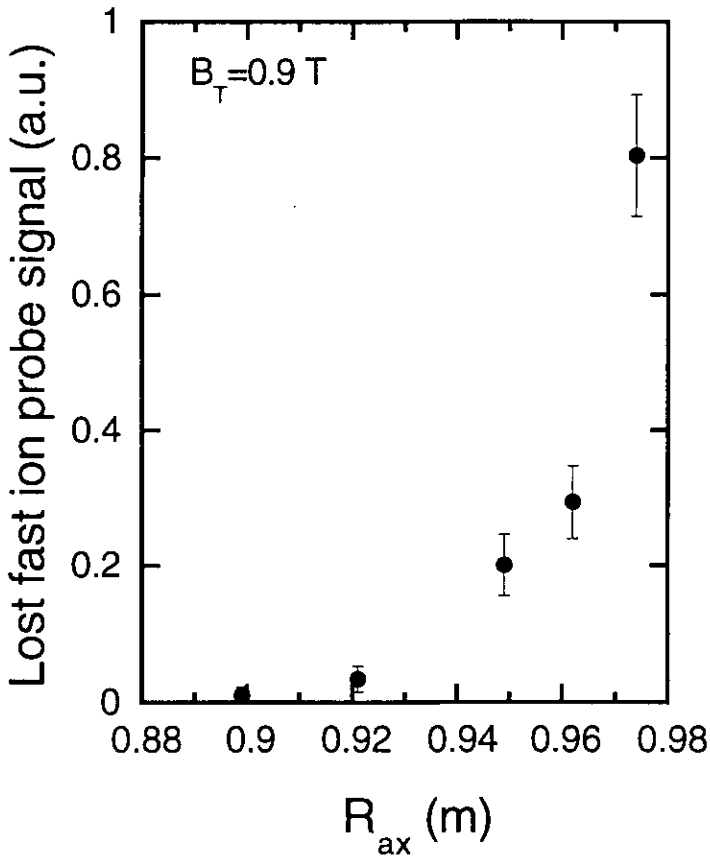

Fig. 28. Dependence of fast ion loss probe signal intensity measured with single channel PMT on R_{ax}. Signal intensity increased drastically as R_{ax} moved to outward (plasmas come close to the probe).

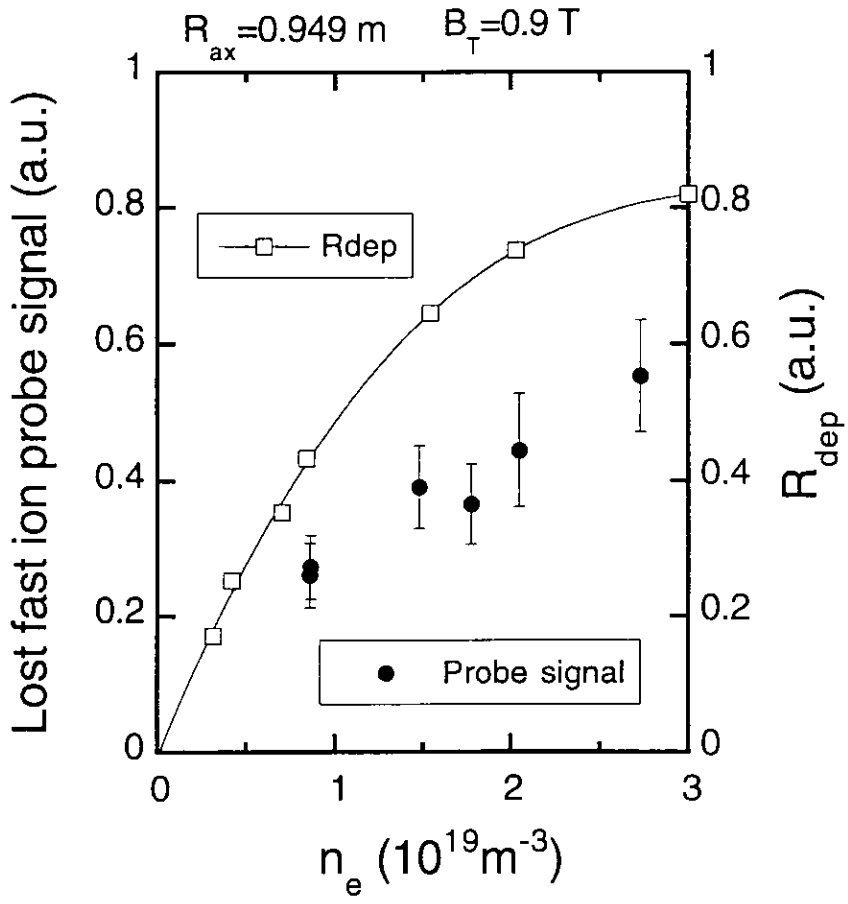

Fig. 29. Dependence of fast ion loss probe signal intensity measured with single channel PMT on n_e together with computed deposition fraction of NB, R_{dep} with the HFREYA code.

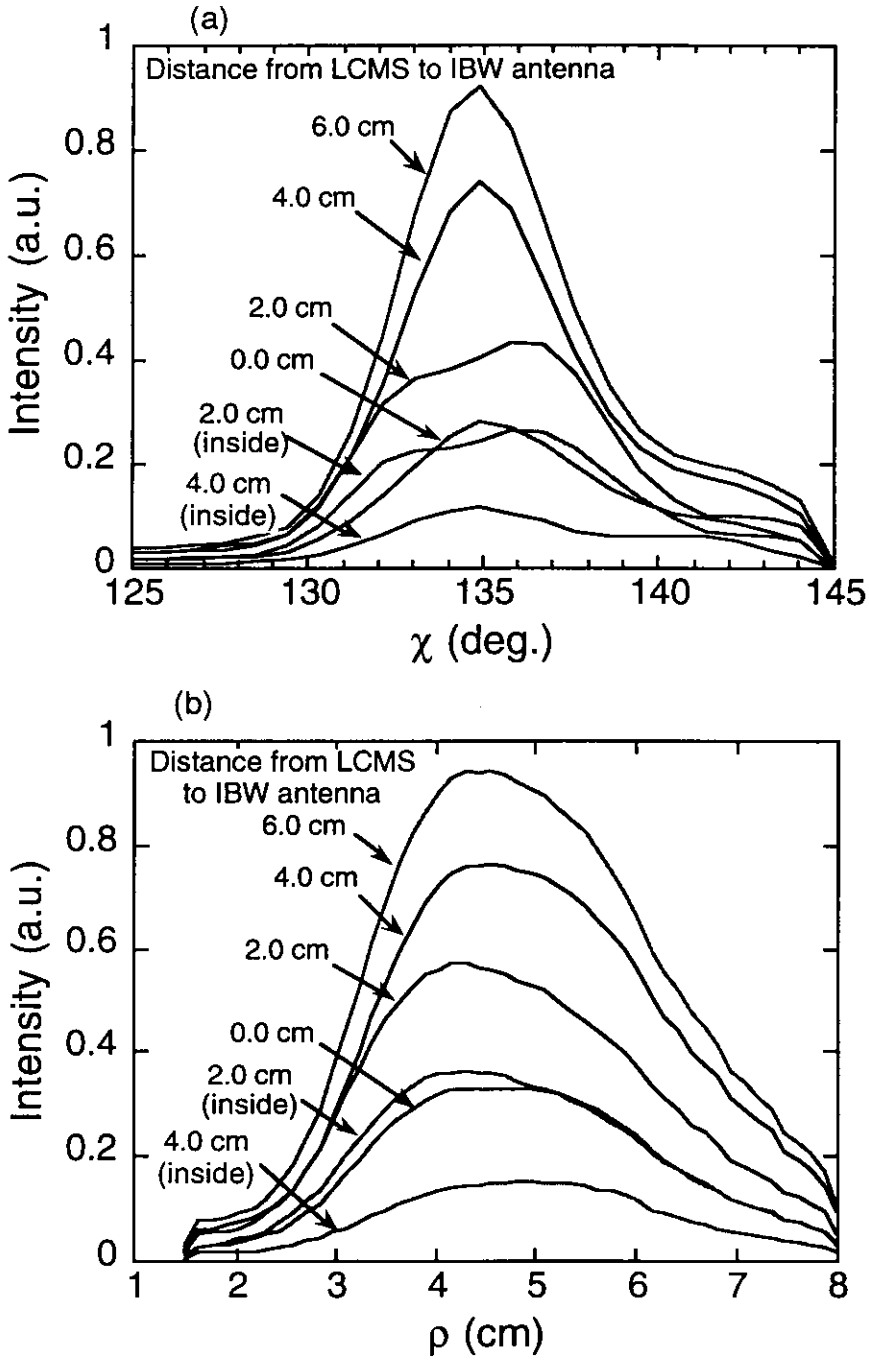

Fig. 30. Influence of the antenna position on fast ion signals, (a)pitch angle distribution and (b)gyroradius distribution of detected ions.

4.2 Classical losses

The fast measurement using the lost-fast-ion probe with multi-channel PMT array was applied to quiescent NB-heated plasmas to investigate classical loss processes [41]. The lost-fast-ion probe with a single channel PMT, which covers whole the area on the scintillator, measures the time behavior of detected ions integrated over χ and ρ_i (Fig. 25). In that measurement, difference of time behavior depending on each of ions with different orbits could not be measured, although dependence of total escaping ion flux on B_T, R_{ax} and n_e were measured (Figs. 27-29). The fast measurement is essential for the investigation of time behaviors of escaping fast ions.

Three classes of loss, χ~135°-140°, χ~130° and χ~110°-120° were typically observed and were identified as losses from passing, passing boundary and trapped orbits, respectively. Figure 31 shows typical χ-ρ_i profiles, (a)B_T =0.9 T and (b)B_T =1.8 T, measured in plasmas with R_{ax} =0.949 m [36]. Signal intensity on the primary loss spot at χ~130° which is due to passing boundary ions in Fig. 31(a) is most intense. In the case of B_T =1.8 T, principal loss of passing boundary ions vanished and loss from trapped orbits was seen clearly.

The different time behaviors of escaping ions, which suggest different classical loss processes, were observed on PMT signals corresponding to passing ions and trapped ions. Typical examples are shown in Fig. 32; (a) a signal of passing ions with χ of 138°±1°, E_i of approximately 38 keV (#71681, R_{ax} =0.974 m, B_T =0.95 T), and (b) a signal of trapped ions with χ of 115°±5°, E_i of approximately 38 keV (#69695, R_{ax} =0.949 m, B_T =1.5 T). The signal of passing ions (a) starts synchronously at the moment of NB injection and slowly rises, while the signal intensity of trapped ions (b) rises gradually in time. The rise time behaviors for both signals, (a) and (b), are different clearly. Loss processes for both kind of ions are discussed in section 5.1.

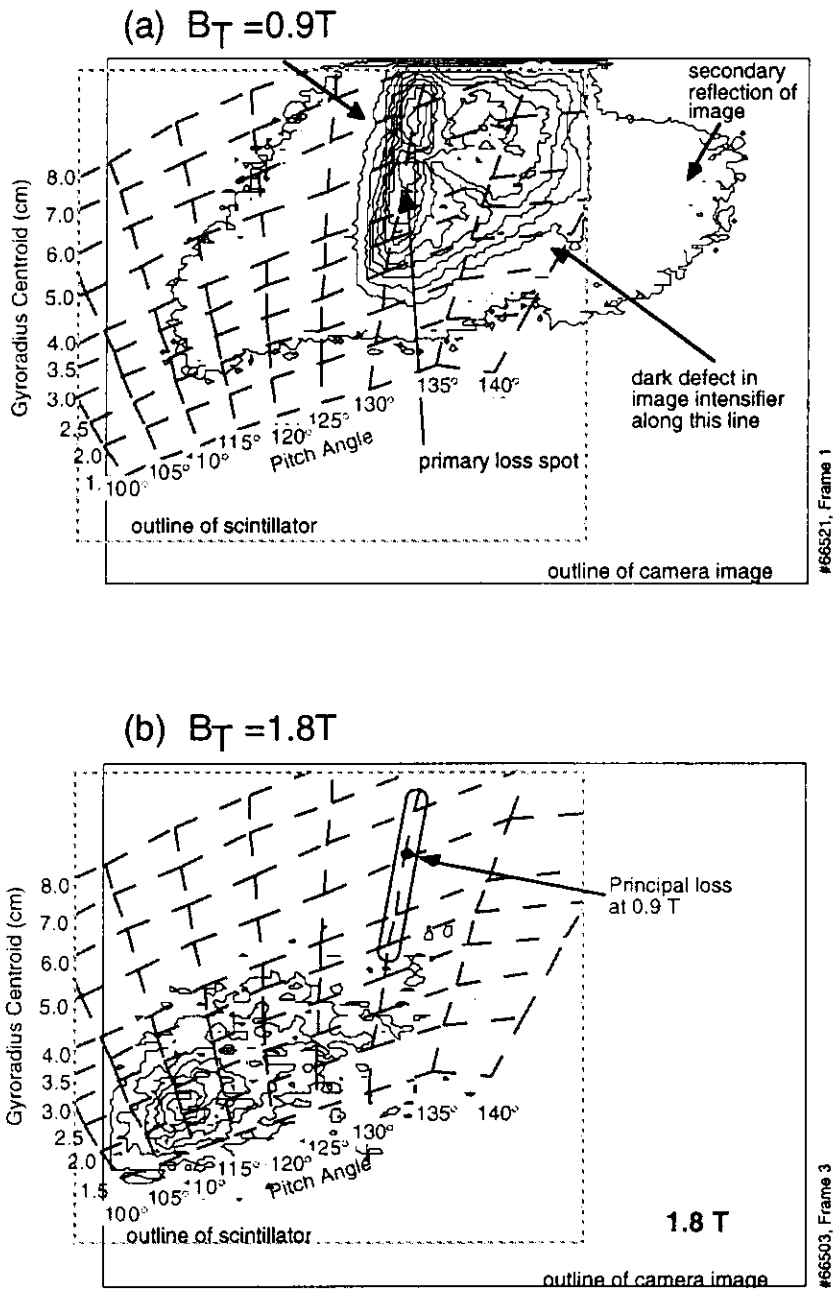

Fig. 31. Typical χ-ρ_i profiles, (a)B_T =0.9 T and (b)B_T =1.8 T, measured in plasmas with R_{ax} =0.949 m [36].

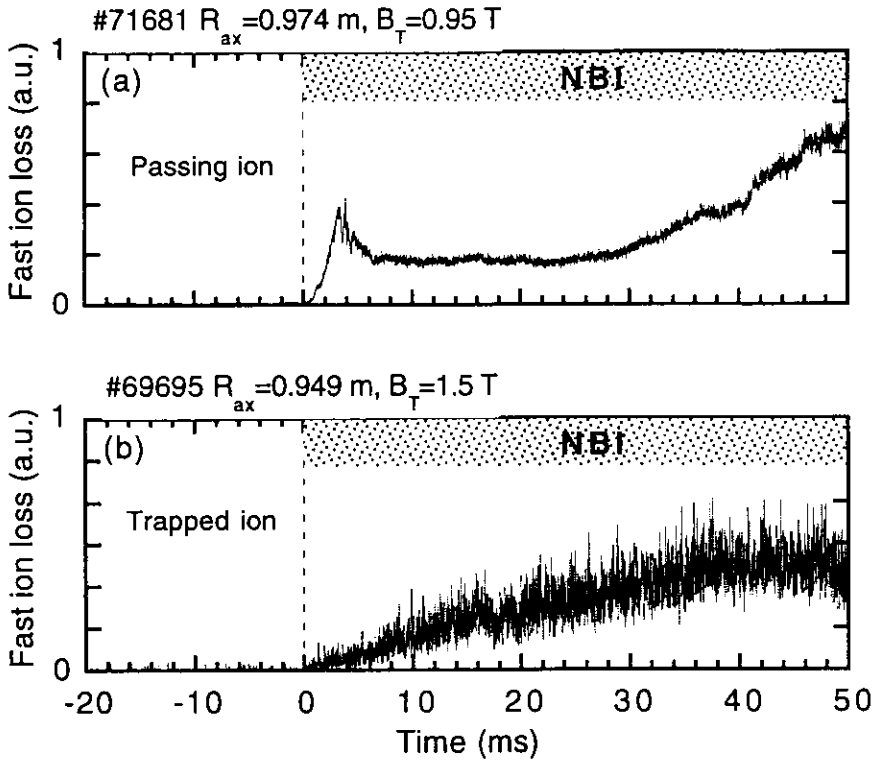

Fig. 32. Time traces of two kinds of escaping ion; (a) co-going passing ions with χ of 138°±1°, E of approximately 38 keV, and (b) co-going transition ions with χ of 115°±5°, E of approximately 38 keV.

4.3 MHD-induced losses

The fast measurement using the lost fast ion probe were carried out for NB-heated plasmas containing fishbone-like modes [42]. The aperture angle was +45° to measure co-going ions and -45° for ctr.-going ions.

In CHS, two types of the fishbone-like instabilities are observed on the magnetic probe array, Langmuir probes, soft-X ray array and HIBP [43,44]. One is the m/n=3/2 fishbone-like instability, which is often observed in discharges with an outward-shifted plasma ($R_{ax} \geq 0.949$ m). The other is the m/n=2/1 fishbone-like instability, which is often observed in discharges with an inward-shifted plasma (R_{ax} =0.921 m). The low magnetic field (B_T~0.9 T), the co-injected NB and the low electron density (n_e ~1.0x10^{19} m^{-3}) are characteristics of these two burst modes. The mode numbers m/n were determined from the phase difference of the magnetic fluctuation measured by the poloidal/toroidal magnetic probe arrays [29]. No such instabilities were observed in ECRH plasmas without NBI. The m/n =3/2 fishbone-like instability has a typical mode frequency of approximately 50-100 kHz. The time trace of a typical discharge is shown in Fig. 33. Burst like spikes in the Mirnov signal appear 30 ms after the beam injection starts and the spikes on the fast ion loss correlate with them. Spikes of both co-going and ctr.-going fast ion loss were observed in plasmas containing m/n =3/2 modes, while no spikes were observed in plasmas containing m/n =2/1 modes. In this thesis, the study is focused on the MHD-induced fast ion losses during the m/n =3/2 mode.

4.3.1 Losses of co-going ions

Time traces of co-going fast ion losses for various pitch angles and gyroradii are shown in Fig. 34 together with those of the magnetic fluctuation observed by a single magnetic probe during the m/n =3/2 burst. The discharge had parameters, R_{ax} =0.995 m, B_T =0.9 T and n_e ~1.2 x 10^{19} m^{-3}. Four signals are shown in Fig. 34 (a) with χ =146°±2°, ρ_i ~3.7 cm, (b) with χ =136°±3°, ρ_i ~5.2 cm, (c) with χ =137°±4°, ρ_i ~1.8

cm and (d) with $\chi = 116° \pm 6°$, ρ_i ~3.5 cm, corresponding to channels 2, 6, 7 and 11 shown in Fig. 22(a) respectively. The largest spikes are seen on the signal of channel 6 (see scale).

Orbit calculations have been performed to investigate the ion orbits detected in channels 2, 6(7) and 11. Figure 35 shows the result of these calculations. In the top right plot, (for co-injected NBI#1), the aperture and the circulation of the injected ions are shown. Figure 35(a) shows a passing orbit of ch.2 with a large pitch angle at the aperture position (142°). Energy of 38 keV which was the injection energy of NBs was used for the calculation because of the poor energy resolution of this probe as shown in Fig. 23(b). The ion continues to circulate in the torus. The orbit in Fig. 35(b) shows a passing boundary orbit of ch.6(7) with a intermediate pitch (133°). It has a reflection point after several poloidal evolutions. To use the energy of 18 keV was determined as follows. Large spikes were seen in ch.6 and ch.7 which cover same pitch angle region ; approximately 136°. The ratio of the amplitude of these spikes in ch. 7 to that in ch. 6 is 1:2, while the ratio is 1:10 for the quiescent portion of the loss signal. The latter ratio corresponds to the distribution of the protons with the energy loss of near its initial energy (38 keV) and the ratio of spikes is corresponding to lower energy protons. If we assume these spikes consist of mono-energetic ions, the ratio of 1:2 can be explained with 18 keV protons due to the energy resolution as shown in Fig. 23(b). Figure 35(c) presents a trapped orbit of ch.11 with a small pitch angle (119°). The ion comes to the probe after the reflection. Energy of 38 keV was used for the calculation as same as the case of Fig. 35(a). Most of the tangentially injected beam ions circulate in the clockwise direction (viewing from the top of the device). When the direction of the aperture is set at 45° relative to the major radial direction of the probe position, it is possible to detect passing ions and passing boundary ions, and trapped ions. It can be seen clearly in Fig. 34 that the signal for passing boundary ions only has large spikes synchronizing with the magnetic fluctuation seen by the magnetic probe, although large spikes are not observed on other signals.

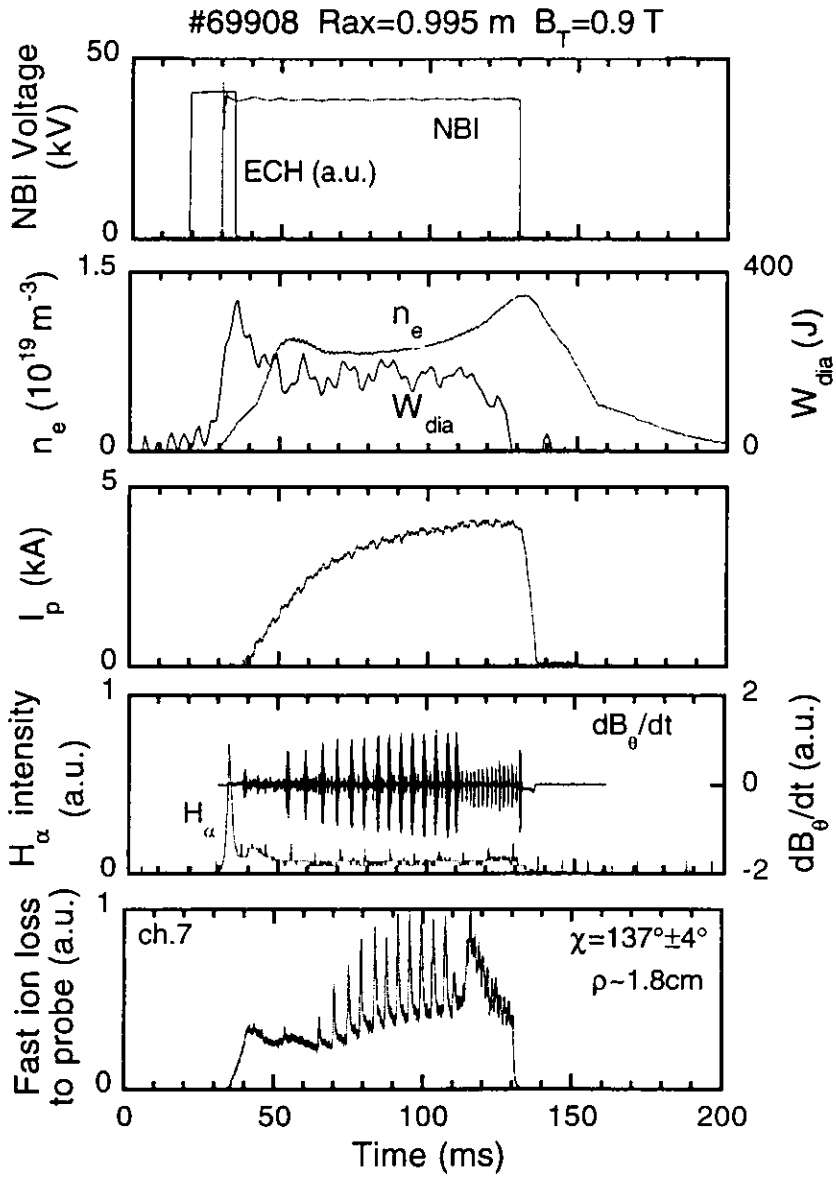

Fig. 33. Time traces of the typical shot when m/n =3/2 fishbone-like burst mode was observed. Duration of ECH and NBI, stored energy W_{dia}, line averaged electron density n_e, plasma current I_p, H_α intensity, magnetic fluctuation and fast ion losses are presented. It is shown that the burst mode emerged in NBI duration.

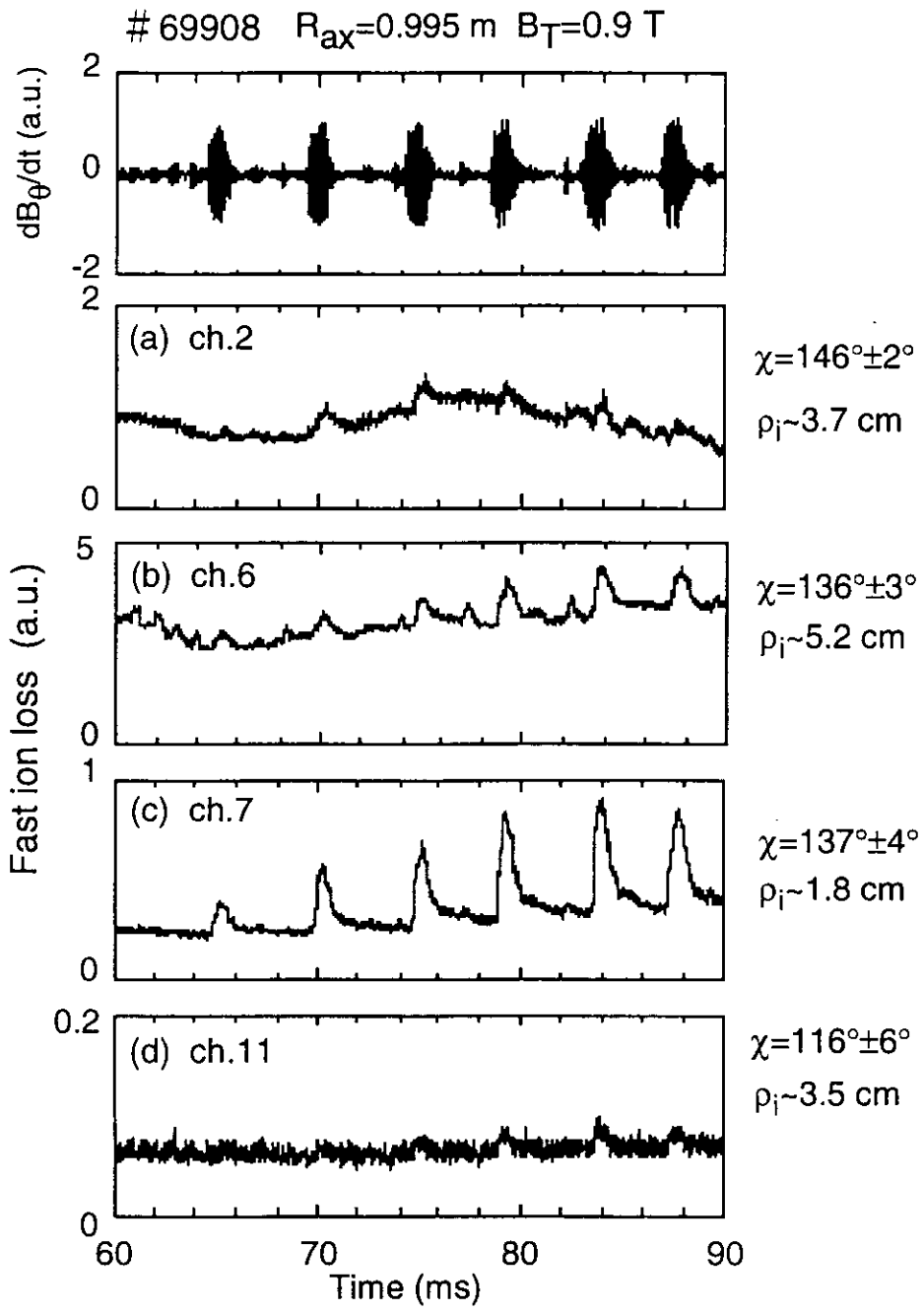

Fig. 34. Time traces of the magnetic fluctuation and fast ion losses of different pitch angle and the gyroradius. Each of channel number corresponds to channel numbers shown in Fig. 21(a). Largest spikes are only seen on the signal of the channel 6 (see scale).

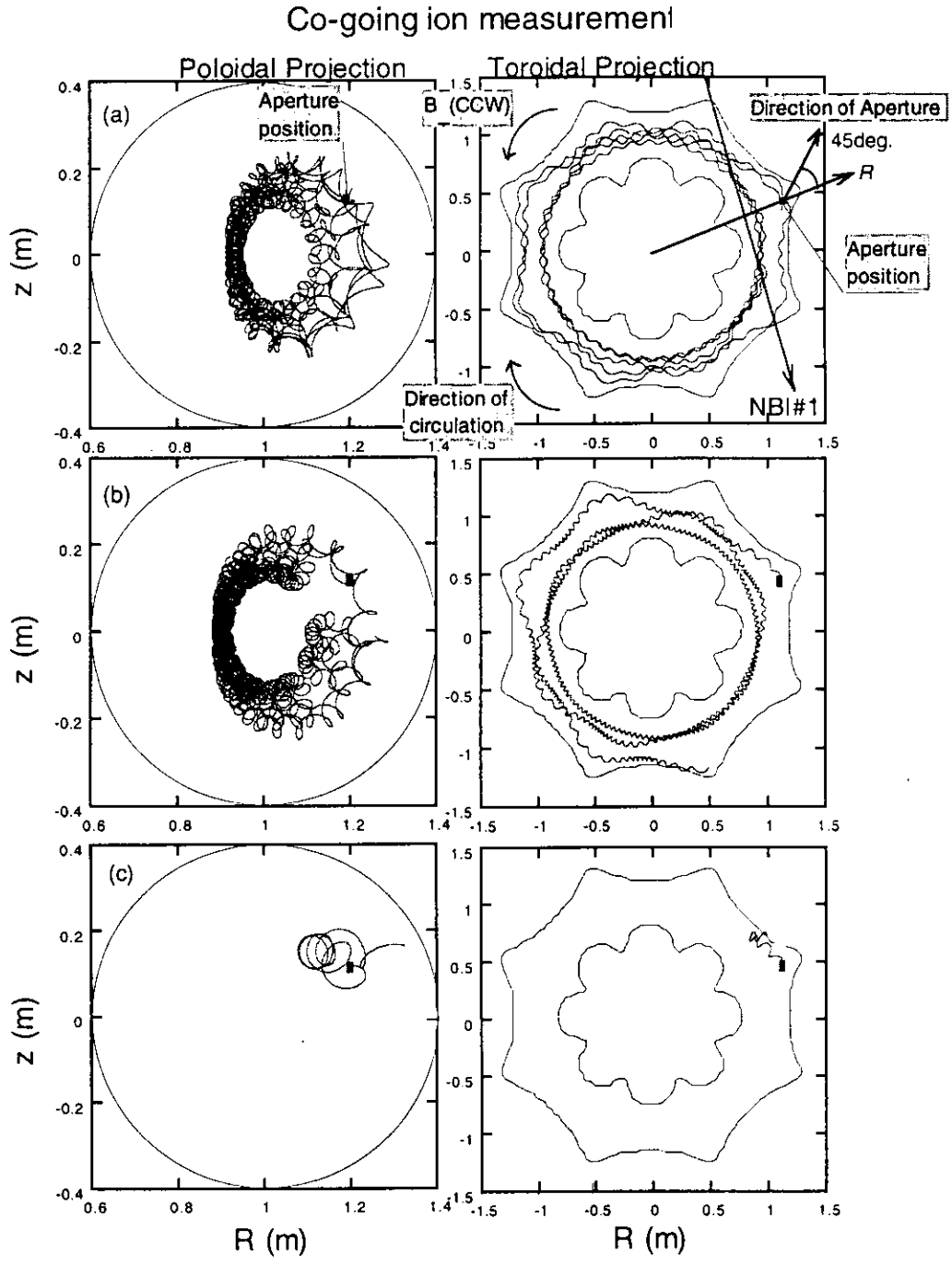

Fig. 35. Orbits of (a) a passing ion with E_i =38 keV, χ =146°, (b) a passing boundary ion with E_i =18 keV, χ =133° and (c) a trapped ion with E_i =38 keV, χ =119°. This calculation is performed with R_{ax} of 0.995 m and B_T of 0.9 T.

4.3.2 Losses of counter-going ions

In a tokamak plasma, trapped ions play an important role in the excitation of MHD instabilities and in the resulting MHD-induced losses. Theories predict that the resonance between the precession frequency of trapped ions and the mode frequency of the MHD instabilities leads to losses of trapped ions [47]. In order to investigate such losses in a heliotron/torsatron type device, measurements of the loss of trapped ions were made. The ninety-degree rotation of the probe itself in the cw direction makes it possible to detect ctr-going trapped ions (-45° of aperture angle). In this case, co-injected beam ions are reflected by the magnetic mirror into the ccw direction and terminate at the probe. Figure 36 shows a bounce orbit of an ion detected by the probe. The direction of the co-injected NBI and that of the aperture are also shown.

Trapped ion losses also occur under the same conditions that produced the passing boundary ion loss. A time evolution of losses of trapped ions with various pitch angles and gyroradii is shown in Fig. 37 together with that of the magnetic fluctuation. The shot had parameters, R_{ax} =0.974 m, B_T =0.9 T and n_e ~1.2x10^{19} m^{-3}. Four signals, a) on ch.7 with χ =63°±13°, ρ_i ~1.8 cm, b) on ch.8 with χ =87°±3°, ρ_i ~2.8 cm, c) on ch.12 with χ =79°±6°, ρ_i ~7.5 cm and d) on ch.6 with χ =42°±6°, ρ_i ~1.0 cm are shown in the figure. The largest spikes are seen in the signal with a pitch angle of approximately 90° and an energy of approximately 20 keV. The enhancement ratio of fast ion loss to base loss level for 90° losses is up to a factor of ~20, while only a factor of ~2 for the case of passing boundary ions. Therefore, it is thought that ctr-going trapped ions are more sensitive than passing boundary ions for MHD instabilities. However, the absolute particle flux of the 90° losses were much smaller than that of passing boundary ions as mentioned in the section 4.3.3.

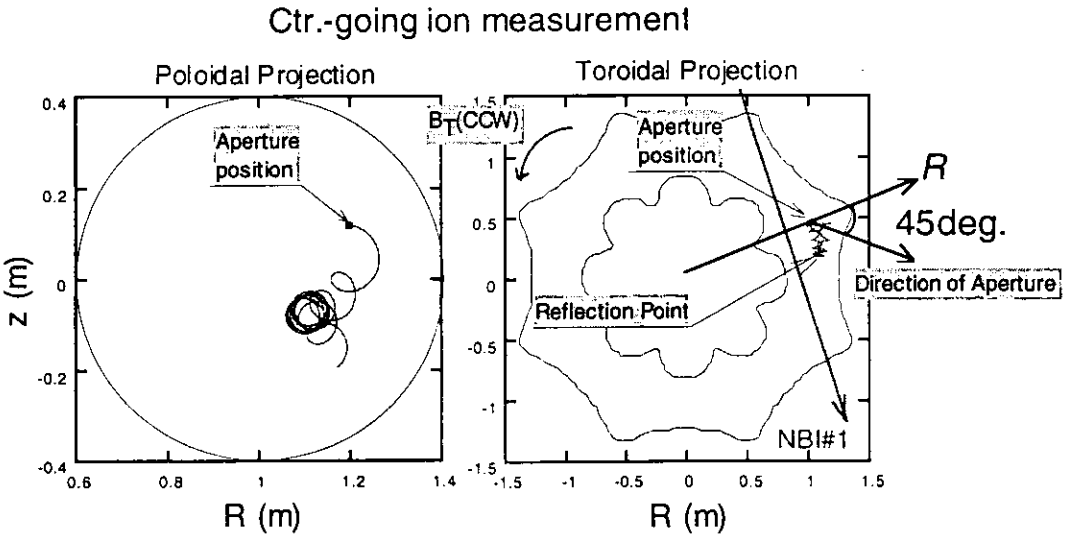

Fig. 36. Orbit of the ctr-going ion with E_i =38 keV, χ =53°, which co-injected beam ions are reflected and come to the probe. This calculation is performed with R_{ax} of 0.995 m, B_T of 0.9 T.

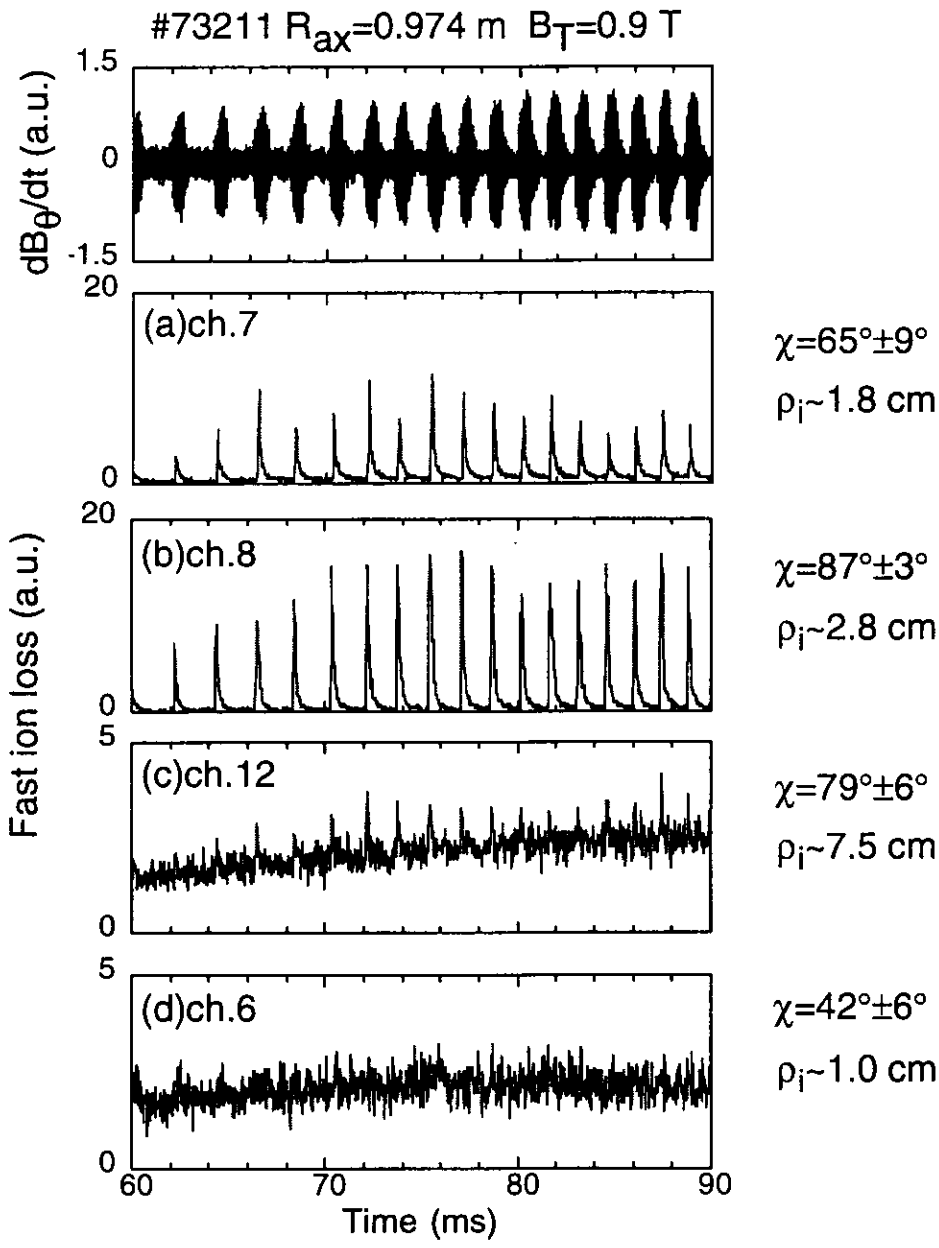

Fig. 37. Time traces of the magnetic fluctuation and fast ion losses with different pitch angle and gyroradius. Largest spikes are seen on the signal of 90° ions.

4.3.3 Comparison of intensity between co- and counter-going ion losses

As seen in previous section, losses of ctr.-going trapped ions were enhanced by a factor of 20 during MHD activity, while those of co-going passing boundary ions were enhanced by a factor of 2 at most. Enhancement ratio of trapped ion losses was 10 times larger than that of passing boundary ions. It was suggested that trapped ions were more sensitive to MHD activity than passing boundary ions. From the view of degradation of heating efficiency or damage to the first wall, information of absolute fast ion loss flux is important. In this section, approximate comparison of signal intensities between co- and ctr.-going ions are made using 2D image data. Figure 38 shows typical 2D χ-ρ_i profiles, (a) for co-going ions and (b) for ctr.-going ions, measured in plasmas with the m/n=3/2 fishbone like instability. Magnetic field configuration was R_{ax} =0.995 m and B_T =0.9 T. It is not adequate to use PMT data for comparison of signal intensities because intense light spots on each of figures were not covered by PMT views. Comparison was made with numerically processed data of digitized 2D images by using the gain curve of image intensifier (Fig. 20). Intensity in the area on the intense spot of co-going ions were approximately 10 times larger than that of ctr.-going ions.

(a) Co-going ion measurement

#69908 , 66.6ms-99.9ms

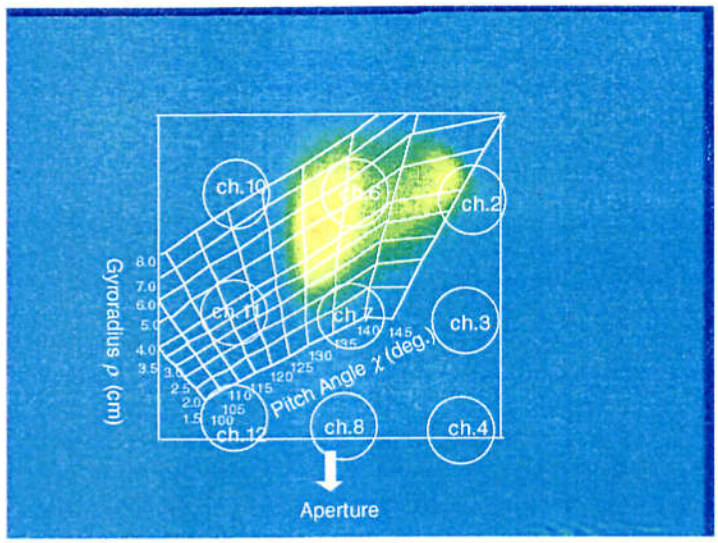

(b) Ctr.-going ion measurement

#74097, 66.6ms-99.9ms

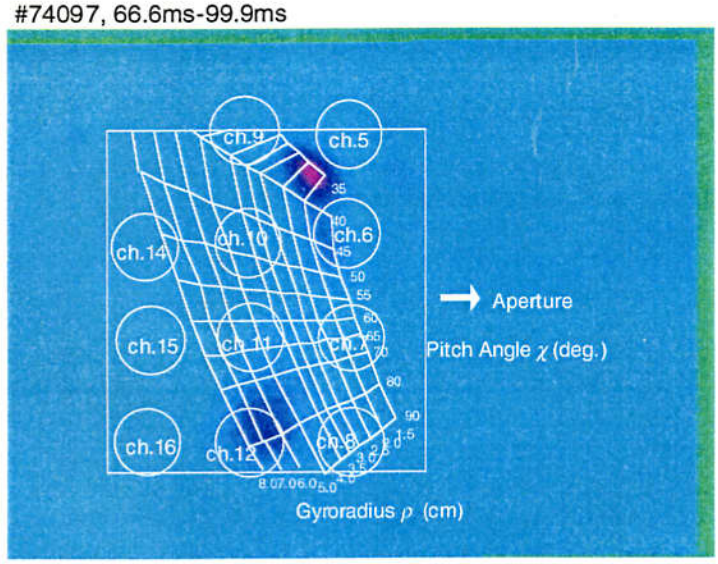

Fig. 38. Typical 2D χ-ρ_i profiles, (a) for co-going ions and (b) for ctr.-going ions, measured in plasmas with the m/n=3/2 fishbone like instability.

4.3.4 Dependence of losses on electron density, neutral beam power and toroidal magnetic field strength

The dependence of co-going passing ion losses upon n_e, power of NB P_{NB} and B_T are shown in Fig. 39. Note that the vertical axes represent the spike amplitude normalized by base level of the loss without spikes. The density dependence of losses is shown in Fig. 39(a). Losses vary with increase of n_e for the NBI duration and are enhanced around n_e of 0.7-1.0 x 10^{19} m^{-3}. Then, the magnetic fluctuation is also increased in this range. Losses vanish when n_e is higher than ~1.3 x 10^{19} m^{-3}, while the magnetic fluctuations, although decreasing with increasing n_e, are still observed. The NB power dependence of losses is shown in Fig. 39(b). The data from 4 shots with different P_{NB} are plotted. The losses and the magnetic fluctuation are enhanced with increasing P_{NB}. For P_{NB} of 0.46 MW, no losses are seen, while the magnetic fluctuation is still observed. Figure 39(c) shows the magnetic field dependence of losses. The magnetic fluctuation is enhanced at 0.9 T drastically, while no such a change is seen for losses. No losses are seen at 1.05 T, while the magnetic fluctuation is still seen.

The dependence of ctr.-going trapped ion losses upon n_e, P_{NB} and B_T are shown in Fig. 40. The vertical axes in these figures also represent the relative value of the spike amplitude correlating to MHD oscillations to the base loss level without MHD oscillations as same as in Fig. 39. Losses and the magnetic fluctuation are observed in the density range, ~0.5 x 10^{19} m^{-3}<n_e<~1.5 x 10^{19} m^{-3}. No losses are seen at the density, n_e ~0.4 and ~1.4 x10^{19} m^{-3}, while the magnetic fluctuation can still be seen. Losses and the magnetic fluctuation are enhanced with increasing P_{NB}. For the power of 0.58 MW, no losses are seen, while the magnetic fluctuation is still observed. In B_T dependence, it is seen that losses vary with magnetic fluctuation amplitude. Losses are seen at B_T =0.95 T together with a small magnetic fluctuation, although losses vanish when the magnetic field is larger than 1.0 T. The dependence of ctr.-going trapped ion losses on these parameters is similar to that of the co-going passing boundary ion losses.

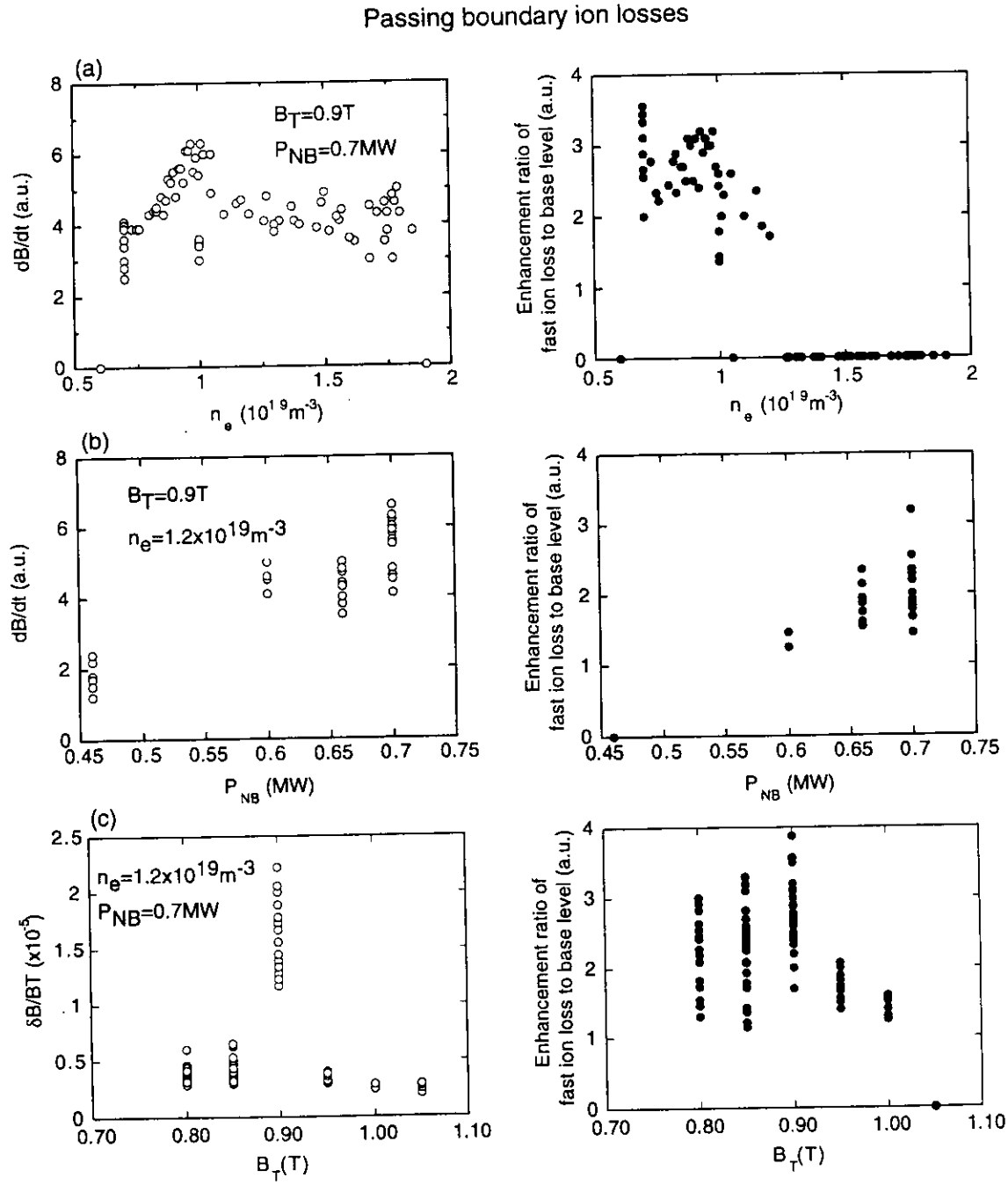

Fig. 39. Dependence of passing boundary ion losses and the magnetic fluctuation on (a) electron density, (b) neutral beam power and (c) toroidal magnetic field.

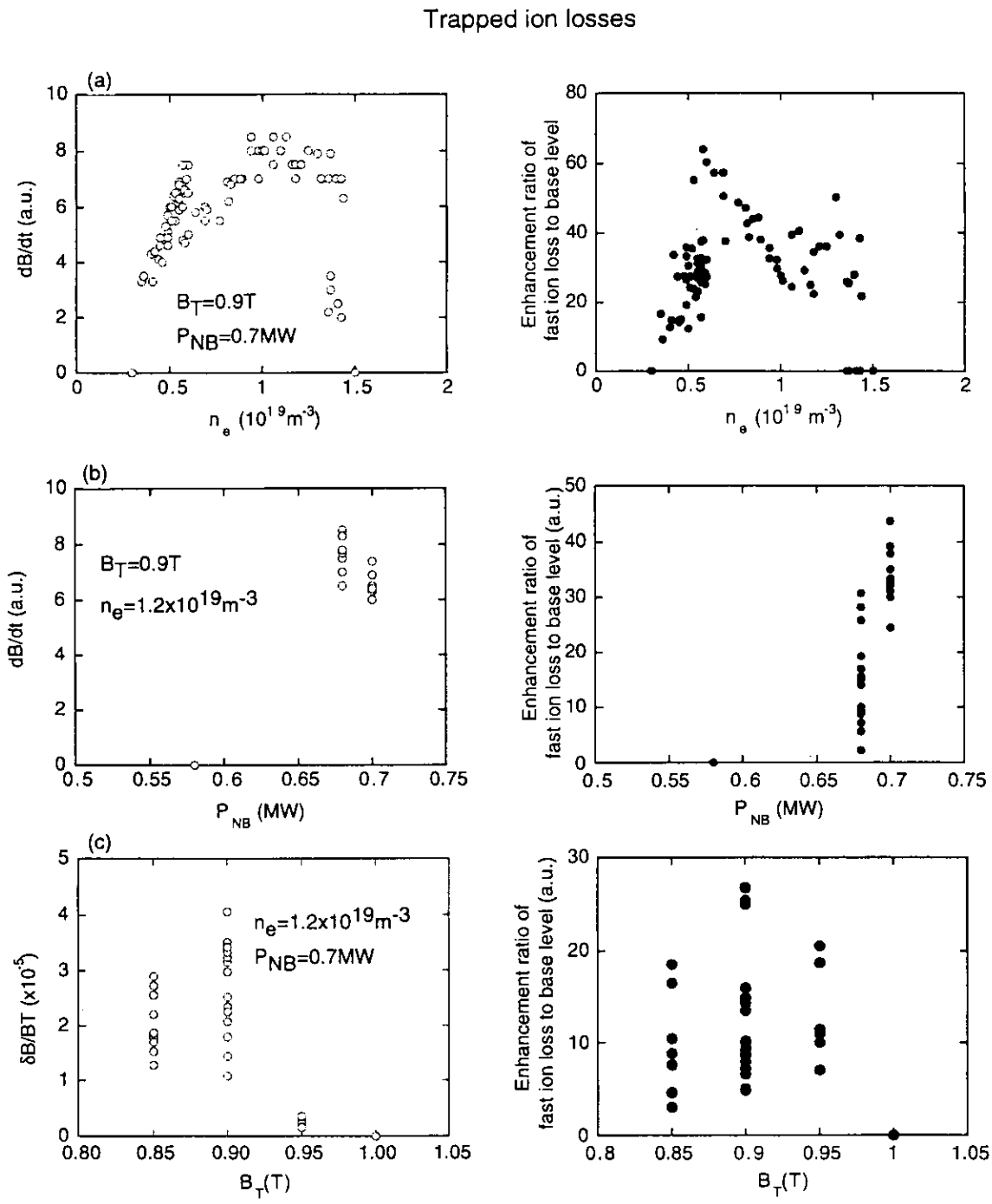

Fig. 40. Dependence of ctr-going trapped ion losses and the magnetic fluctuation on (a) electron density, (b) neutral beam power and (c) toroidal magnetic field.

4.4 Other enhanced losses

4.4.1 Losses due to ECH superimposition

Other types of enhanced fast ion losses, other than classical losses and MHD-induced losses presented in previous section, were observed in CHS. Fast ion losses were enhanced in NB heated plasmas superimposed by ECH. Figure 41 shows the time traces of fast ion loss for plasmas with ECH. Magnetic field configuration was R_{ax} of 0.949 m and B_T of 0.9 T. The plasmas were initiated by ECH and were heated by following NBI. Second ECH pulse was superimposed from 61.5 ms to 66.0 ms. During the ECH pulse, fast ion losses increased by a factor of 4. The enhancement factor of 2~4 was typically seen for ECH superimposed plasmas. It was observed that when ECH was applied, the electron density decreased due to losses of electrons and positive radial electric field, whose radial profile ranged from 0 to +40 V/cm depending on injected power of ECH, was formed [48]. It would be thought that fast ion losses were enhanced by the formed "positive" radial electric field (negative electric field is formed in NBI plasmas) or by the change in the plasma density profile, although the loss mechanism has not been understood yet.

4.4.2 Losses during pellet injection

Enhancement of fast ion losses was observed at the moment of carbon pellet injection. Figure 42 shows time traces of fast ion signal observed on the three channel of the PMT array, (a) with χ =134°±3°, ρ_i ~5.5 cm, b) with χ =136°±5°, ρ_i ~1.8 cm and (c) with χ =115°±6 °, ρ_i ~3.3 cm, together with time trace of n_e during carbon pellet injection. Magnetic field configuration was R_{ax} of 0.949 m and B_T of 1.5 T. The CI signal, which measures the ablation cloud of injected pellet, indicates the timing of pellet injection. Signal intensity of (a) started to rise just after the pellet injection with a delay time τ_{delay} of 0.01 ms and increased to the peak steeply with a rise time τ_{rise} of

0.44 ms. After the peak, the signal intensity decreased with an e-folding time $\tau_{1/e}$ of 0.33 ms. Time behavior of signal (c) of ions with smaller $v_{//}$ differed from that of signal (a) of ions with larger $v_{//}$. Signal intensity of (c) started to rise after the pellet injection with τ_{delay} of 0.40 ms and increased to the peak with τ_{rise} of 0.44 ms. The signal intensity decreased gradually in time with $\tau_{1/e}$ of 1.9 ms. Fast ion losses on signal (a) were enhanced by a factor of 6, while enhancement ratio for signal (c) were 2 at most. Absolute intensity of signal (a) was two times larger than that of signal (b). These time behaviors suggest that these losses are due to pitch angle scattering losses. It is thought that other mechanisms relate to these losses. Pellet-induced losses were explained qualitatively by means of an orbit calculation [49]. Charge exchange neutral particle flux measured with a neutral particle analyzer which has a tangential view line crossing pellet trajectory increased during pellet injection. This indicates that the beam ion loss was enhanced due to redistribution of fast ions because of charge exchange with neutral clouds of ablated pellet.

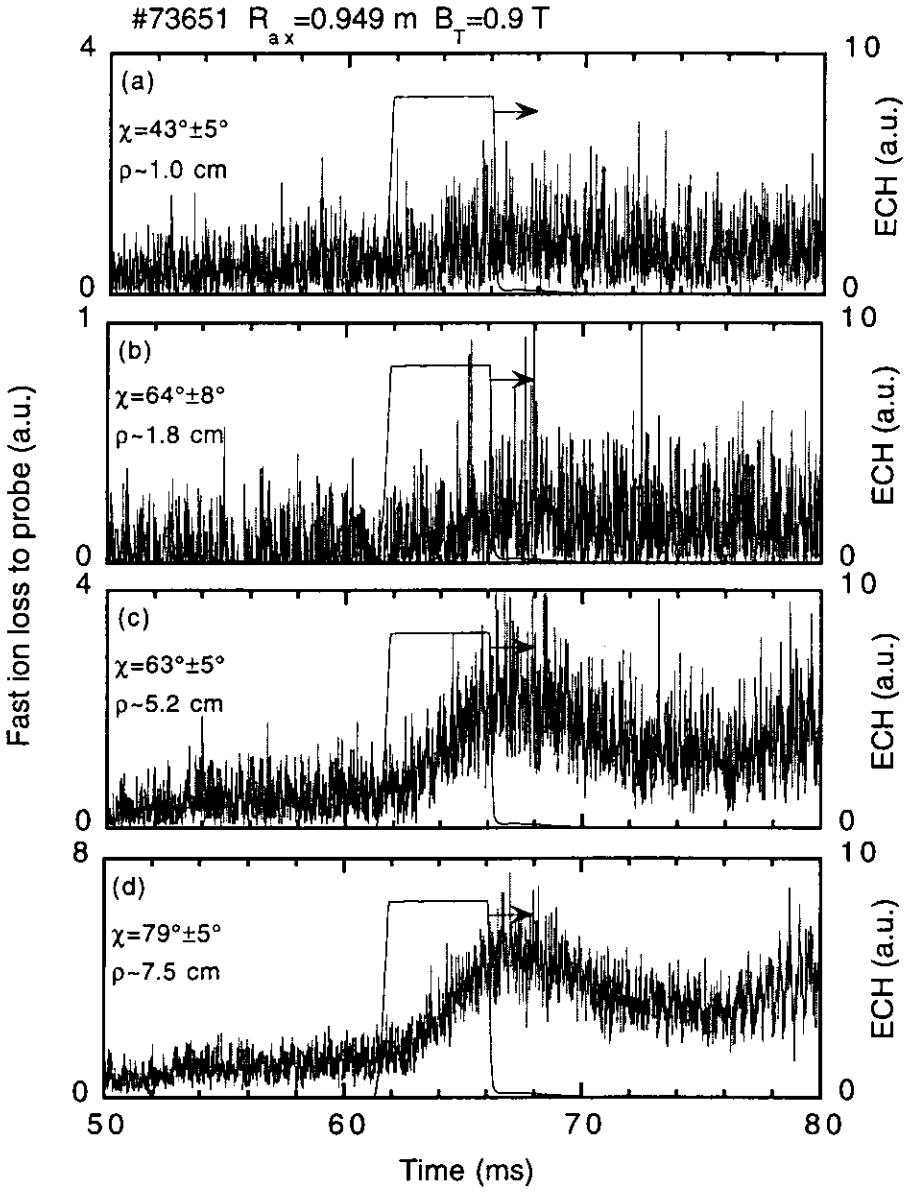

Fig. 41. Time traces of fast ion loss for plasmas with ECH superimposition.

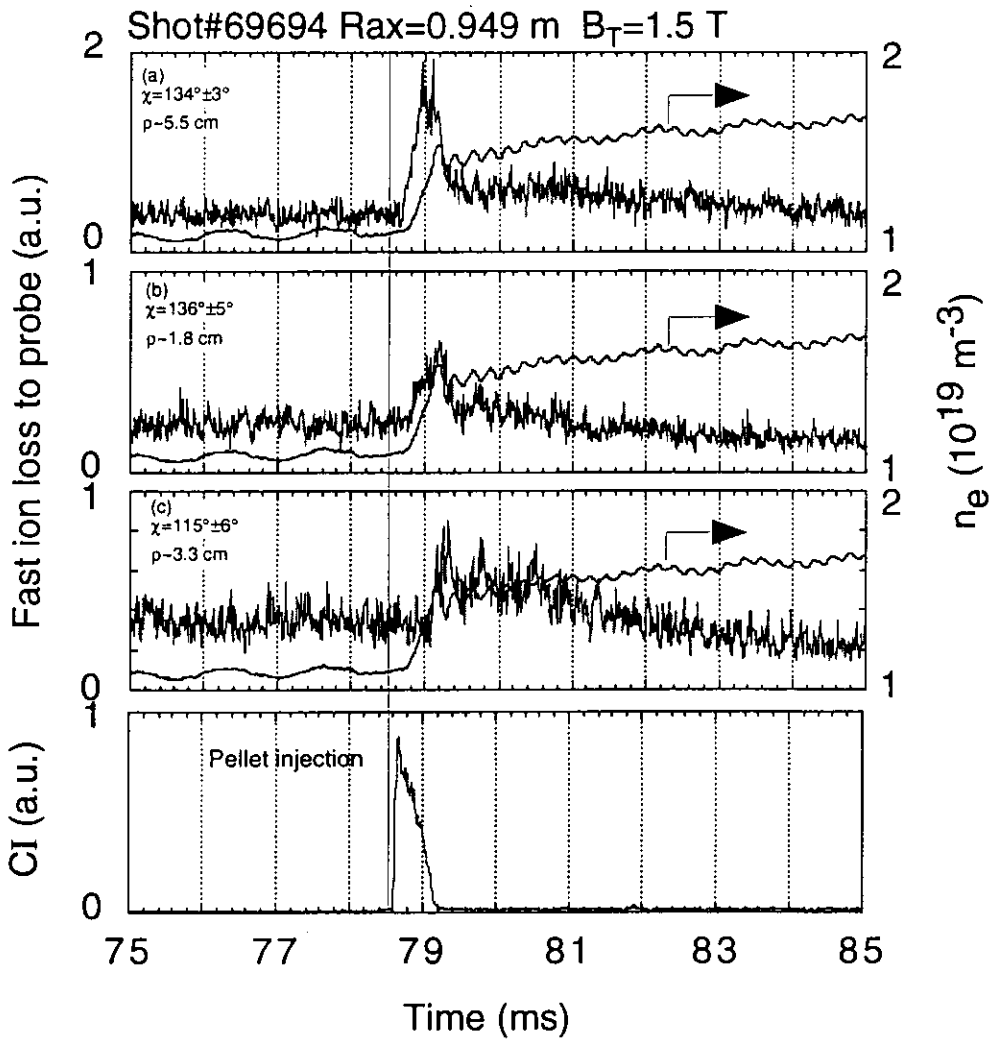

	(a)	(c)
τ_{delay}	0.01ms	0.40ms
τ_{rise}	0.44ms	0.61ms
$\tau_{1/e}$	0.33ms	1.9ms

Fig. 42. Time traces of fast ion signal observed on the three channel of the PMT array, (a) with χ =134°±3°, ρi ~5.5 cm, (b) with χ =136°±5°, ρi ~1.8 cm and (c) with χ =115°±6 °, ρi ~3.3 cm, together with time trace of *n*e during impurity pellet injection.

Chapter 5

Discussions

5.1 Estimation of classical losses

Different time behaviors of passing and trapped ion were derived by using this fast measurement as presented in Fig. 32. Passing ion signal consists of two components; initial steep rising part and following slowly rising one, although trapped ion signal rises gradually in time. The signal intensity of passing ions always rapidly increased with NBI, independently n_e. To reveal the loss process of trapped ions, dependence of the rise time for trapped ion signals on n_e was investigated as shown in Fig. 43. Deflection time, which is mean time for 90° scattering as a typical parameter indicating collision effect, is also presented as a curve to compare with the tendency of dependence of observed rise time on n_e. The value of deflection time plotted in the figure is multiplied by a factor of 0.5 for plotting in same range of rise time for comparison. Presented deflection time was calculated with the effective ionic charge of 3, ion and electron temperatures of 200 eV which were measured values at the beginning of NBI discharges. Rise time of trapped ion signals was inversely proportional to n_e and showed similar tendency to that of the calculated deflection time. Calculated initial pitch angles of deposited NBs on magnetic axis by using the HFREYA code are approximately 150°. Estimated mean pitch angle of detected trapped ions on their orbits by using the orbit code are approximately 120°. In rough estimation, approximately 30° scattering is needed to transfer a deposited ion to a loss orbit reaching the probe. Time for 30° scattering is not largely different from the deflection time multiplied by a factor of 0.5. It is suggested that loss process of passing ions has no relation to collisions, while that of trapped ions with higher χ is related to collisions. Therefore, it is thought that the former is due to the prompt loss

and the latter is due to the collisional pitch angle scattering loss depending on n_e.

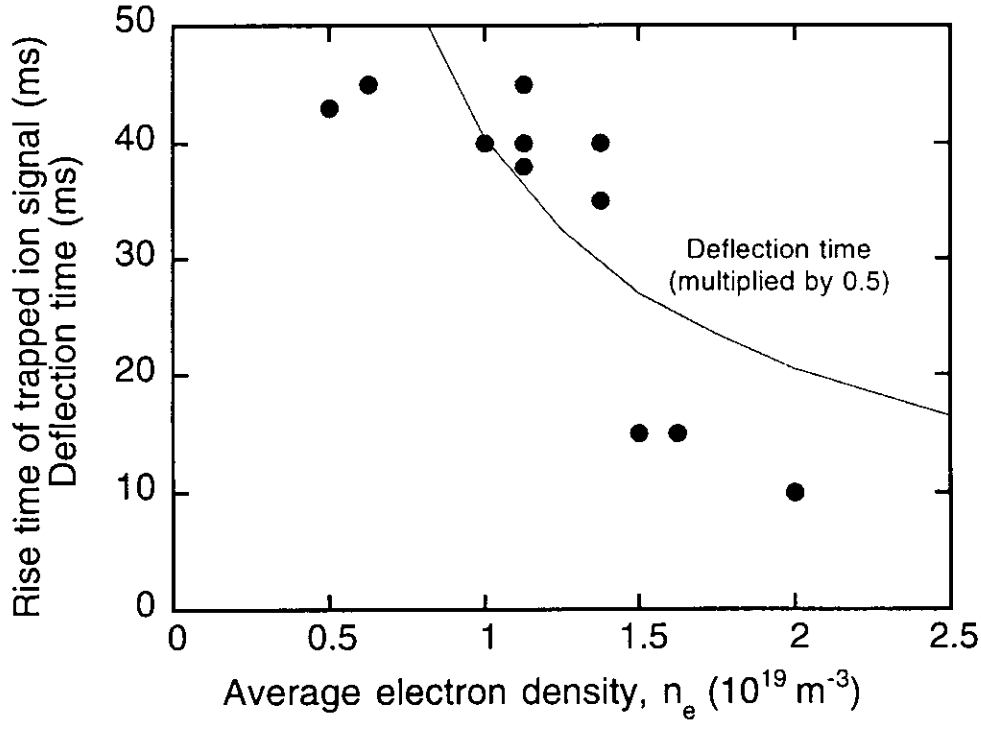

Fig. 43. Dependence of the rising time on n_e. The calculated deflection time (Z_{eff}=3) is also plotted as a curve. The electron density is measured on the central chord.

5.2 Relationship between MHD-induced losses and beam accumulation in plasmas

The instability driven by beam ions and beam ion losses caused by the instability have been presented in section 4.3. The relationship between MHD-induced losses and the mode amplitude of the instability at R_{ax} =0.995 m and B_T =0.9 T is shown in Fig. 44. The enhancement ratio of losses of ctr-going trapped ions was up to a factor of 30 and increased with mode amplitude. On the other hand, the enhancement ratio of losses of co-going passing boundary ions was a factor of 2 at most and was saturated with increasing the mode amplitude. However, the absolute quantity of MHD-induced loss (amplitude of spikes) of co-going passing boundary ions was approximately 400 times larger than that of the ctr-going trapped ions. For the case of passing boundary ions, typical ratio of MHD-induced loss flux to the steady loss flux to the probe was approximately less than 10 %. An influence of MHD-induced losses on stored energy was not seen. For example, difference of stored energy between a plasma with MHD-induced losses (#71790) and that without one (#71791) was approximately 10 %, which was attributable to difference of n_e. A threshold in the mode amplitude of $\delta B/B_T$~3 x 10^{-5} at R_{ax} =0.995 m and B_T =0.9 T was observed for both kinds of ions. This threshold depends on R_{ax} and B_T as seen in Figs 39(c) and 40(c).

In order to interpret the density dependence and NB power dependence of the MHD-induced losses, a possibility that the fishbone-like instability and losses are caused by the accumulation of fast ions in the plasma is examined. Figure 45 shows the correlation of the magnetic fluctuation, losses and plasma current to the accumulation of beam ions, A_{beam}, which was estimated by the following simple expression assuming a steady state condition,

$$A_{beam} = I_{beam} R_{dep} S \qquad (5)$$

Here, I_{beam} and R_{dep} are the injected current of the NB and the deposition fraction of the NBs, respectively in plasmas computed with the HFREYA code. The stacking factor S [50], which represents the accumulation of circulating beam ions during the

slowing down time in the torus, is defined by the following formula,

$$S = \frac{v_{beam}\tau_{slow}}{2\pi R} \tag{6}$$

where, v_{beam} and τ_{slow} are the velocity and the slowing down time [51] of beam ions, respectively. Losses and the magnetic fluctuation emerge at A_{beam} ~100 kA, and are enhanced with increasing A_{beam}. The plasma current indicating the accumulation of beam ions is also enhanced with increase of A_{beam}. It is suggested that the fishbone like instability is excited by the presence of beam ions and MHD-induced losses are caused by the instability. The dependence of losses on P_{NB} is explained by the correlation to A_{beam} (Fig. 45). The density dependence of losses (Figs. 39(a) and 40(a)) can also be interpreted. In a low density plasma, A_{beam} is low because of the low R_{dep}. On the other hand, in the higher density plasma, A_{beam} is low because of the shorter τ_{slow} whilst R_{dep} will saturate. Therefore, there exists a density region with the largest loss for the observation of MHD-induced losses.

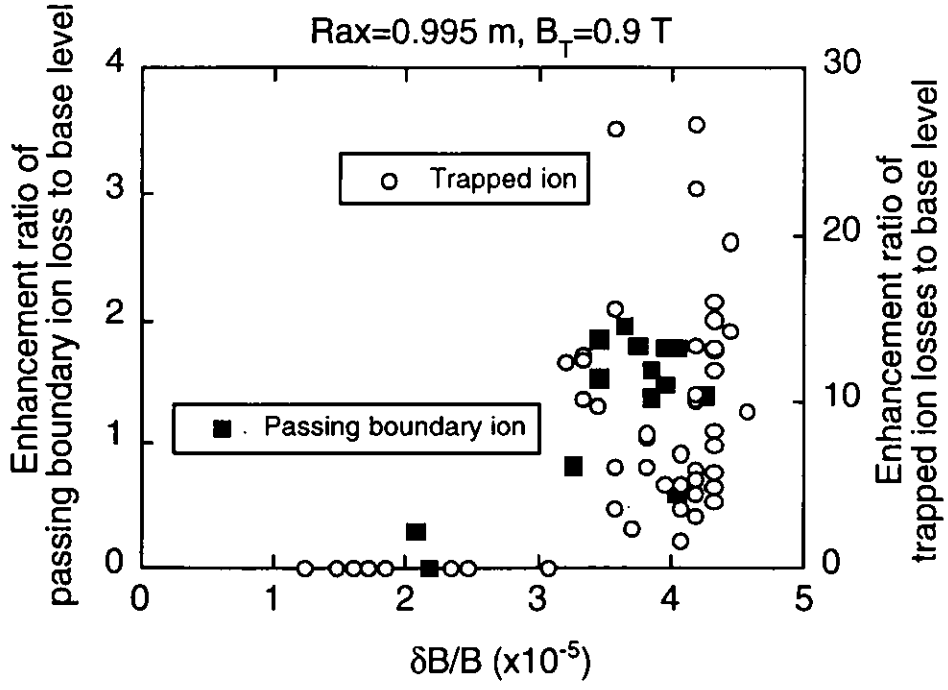

Fig. 44. Relationship between enhancement ratio of ion losses and the mode amplitude of instability at R_{ax} =0.995 m, B_T of 0.9 T. Absolute quantity of MHD-induced loss (amplitude of spikes) of co-going passing boundary ions was approximately 400 times larger than that of ctr-going trapped ions. Losses of ctr-going trapped ions are enhanced as the mode amplitude increases, while those of passing boundary ions are saturated. The threshold in the mode amplitude to losses is seen.

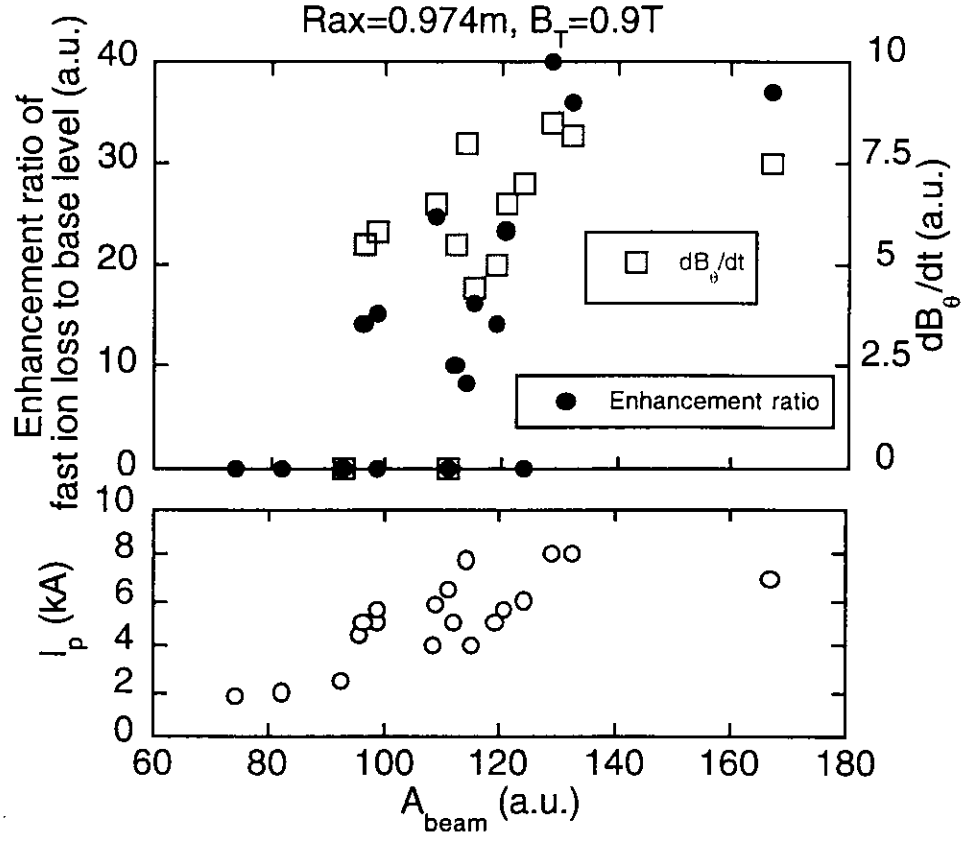

Fig. 45. Correlation of losses, the magnetic fluctuation and the plasma current to the accumulation of beam ions A_{beam} in plasmas. Losses and the magnetic fluctuation emerge at A_{beam} ~100, and are enhanced with increase of A_{beam}. It is suggested the fishbone like instability and MHD-induced losses are excited by the presence of beam ions.

5.3 Interaction between fast ions and MHD modes

The periodic beam ion losses correlating with MHD oscillation were observed on the signals of co-going passing boundary ions and ctr.-going trapped ions with the energy lower than injection energy during the m/n=3/2 fishbone like instability in CHS. To see the fast time behavior, the enlarged fast ion loss signals for both kinds of ion with magnetic fluctuation are shown in Fig. 46. The discharges had the following parameters; R_{ax} =0.974 m, B_T =0.9 T and n_e ~1.2x10^{19} m^{-3}. Figure 46(a) shows co-going passing boundary ion signal with χ of 138°±1°, E_i of approximately 38 keV. The fast ion loss signal starts when the magnetic fluctuation amplitude reaches the maximum level and the magnetic fluctuation starts to decrease after the ejection of fast ions. The ctr.-going trapped ion signal with χ of 87°±3°, E_i of approximately 20 keV is presented in Fig. 46(b). Trapped ions are ejected before the magnetic fluctuation amplitude reaches the maximum level. The difference of the time lag in two kinds of ejection is seen in most cases. The correlation between the time from the start of a burst to the start of ejection and the fluctuation amplitude when the fast ion ejection starts is shown in Fig. 47. The tendency that trapped ion losses arise earlier than passing boundary ion losses is seen. It is thought that the tendency is not due to difference of the energy for both kinds of ion and is due to the difference of their orbits, because it was observed that trapped ion losses on different three channels started simultaneously. The tendency does not depend on the magnetic fluctuation frequency.

It is predicted theoretically in tokamaks that the transit frequency of the toroidally circulating ions or the precession frequency of the toroidally trapped ions resonates with the rotation frequency of the MHD modes [47, 52-54]. The velocity of an ejected ion in the toroidal direction, V_ϕ and the propagation velocity of the magnetic fluctuation in the toroidal direction, V_B were compared using the orbit calculation code. Figure 48(a) shows the variation of the velocity in the toroidal direction and the position represented by ρ for the orbit of a passing boundary ion in Fig. 35(b). The magnetic fluctuation is not included in this calculation. Horizontal axes represent calculation steps that correspond to the time and the distance. Each of the variations consists of three

periods and they reflect the variation of χ. The slowest period which is seen as three envelopes in the figure is due to the movement of the ion between the outside and the inside of the torus. The medium period, which is seen as the ten peaks in envelopes, is due to the movement of the ion, as it passes through a horizontally and vertically elongated cross section in turn. The fastest period, which is seen within each peak, is due to the Larmor gyration. The phase propagation velocity observed in the magnetic fluctuation was, $V_B = 1.2 \times 10^5$ m/s, in this case and is presented as a line in the graph of V_ϕ. In the variation of V_ϕ, there are points where V_ϕ of the passing boundary ion is close to V_B near the magnetic surface with m/n =3/2 when the ion has large pitch angle. Similar calculations for the passing ion orbit in Fig. 48(b) shows that V_ϕ does not match V_B although the ion passes through the magnetic surface with m/n =3/2. From these, two interpretations for the resonant loss mechanism of passing boundary ions can be proposed. One is that confined passing boundary ions resonate with the propagating wave of the magnetic fluctuation and then, these resonant ions are moved into the loss cone. The other is that confined trapped ions are moved into escaping passing boundary orbits by the magnetic fluctuation at reflection points ($v_{//} \sim 0$). Sanuki et al. studied the spatial structure of loss cone in an l=2 helical system [35]. A particle loss diagram in pitch angle and normalized radius shows that the loss boundary of passing ions approaches the inner region of the plasma as $v_\perp / v_{//}$ increases. Therefore it is possible that even trapped ions confined in the inner region are moved into escaping passing boundary orbits. Same orbit calculation for trapped ion losses as shown in Fig. 48 has been performed, but the orbit length are not long enough to study the resonance condition.

Next, a loss mechanism of trapped ions is discussed. Beam ions are expelled after a certain time from the start of the magnetic fluctuation as shown in Fig 46. The fluctuation frequency changes during one burst [43], but here the frequency at the start of beam ion loss, approximately 35 ~ 55 kHz, is compared with the toroidal precession frequency and the thermal ion diamagnetic frequency. In CHS, the toroidal precession frequency for deeply trapped ions estimated by an analytical formula [55] would differ

from the real toroidal precession frequency because of complicated orbits due to the helical ripple. Therefore, the toroidal precession frequency was estimated by using the orbit calculation. The estimated toroidal precession frequency ranges from approximately 30 to 45 kHz and is close to the observed fishbone frequency when particle ejection starts. However these ranges of frequency are usually different from observed one when the burst starts. This can be understood that fraction of helically trapped beam ions may be too small and to destabilize the present mode in CHS. The estimated diamagnetic frequency was approximately 300 kHz, which is 5 times larger than the observed frequencies.

It can be thought that both the MHD-induced passing boundary ion loss and the trapped ion loss relate to these resonant conditions for their loss mechanism. Further analysis and study of the role of particle-wave interaction on destabilization are needed.

In CHS, the m/n =3/2, m/n =2/1 fishbone-like instabilities and TAE are observed in NBI heated discharges [43,56]. Clear spikes on fast ion losses due to MHD activity were only seen in plasmas with R_{ax} =0.974 m and 0.995 m during m/n =3/2 fishbone-like instabilities. The m/n =2/1 fishbone-like instability is observed with $R_{ax} \leq 0.921$ m. One possible reason for the absence of spikes of fast ion loss during the m/n =2/1 mode is that passing boundary ions do not reach the probe in plasmas with $R_{ax} \leq 0.921$ m because the LCMS of such plasmas is far from the probe position. This was confirmed by orbit calculations for passing boundary ions. TAEs are observed in beam heated plasmas with R_{ax} =0.921 m and 0.949 m. In plasmas with R_{ax} =0.921 m, the reason for no MHD-induced losses would be same as that for the m/n =2/1 mode. For R_{ax} =0.949 m, passing boundary ions can reach the probe. One possible reason for the absence of MHD-induced loss at R_{ax} =0.949 m is that the mode amplitude of the TAE ($\delta B/B_T \sim 10^{-6}$), which is smaller than that of the fishbone-like instability ($\delta B/B_T \sim 10^{-5}$), is less than the threshold for the MHD-induced loss. It might also be speculated that the passing boundary ions and trapped ions are unable to resonate with the TAE mode.

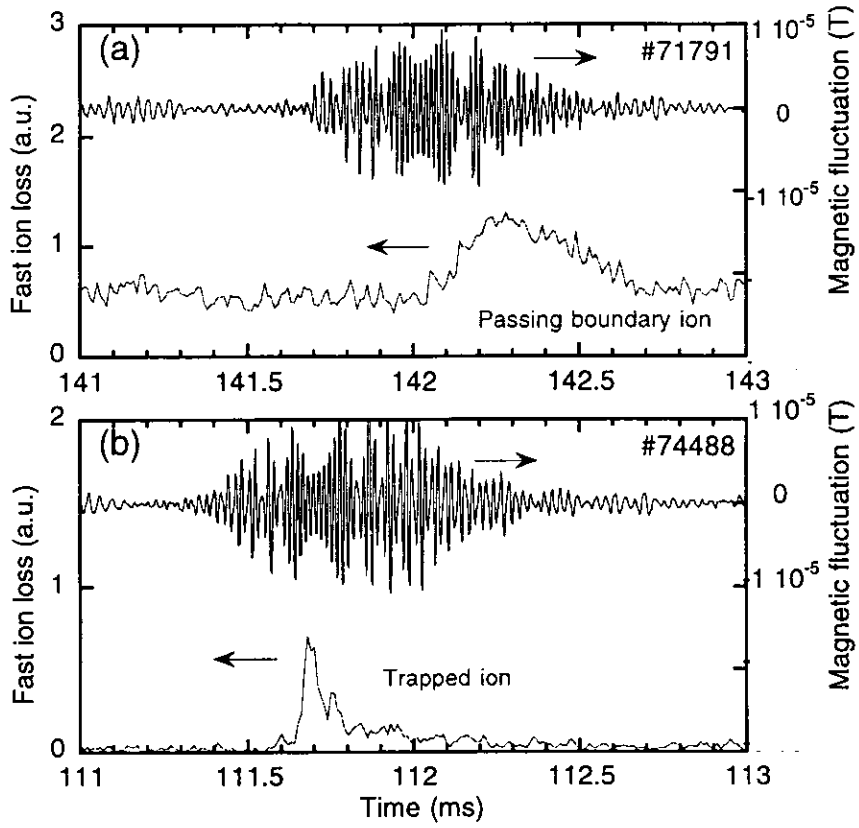

Fig. 46. Enlarged fast ion loss signals with magnetic fluctuation for (a) co-going passing boundary ions with χ of 138°±1°, E of approximately 38 keV, and (b) ctr.-going trapped ions with χ of 87°±3°, E of approximately 20 keV.

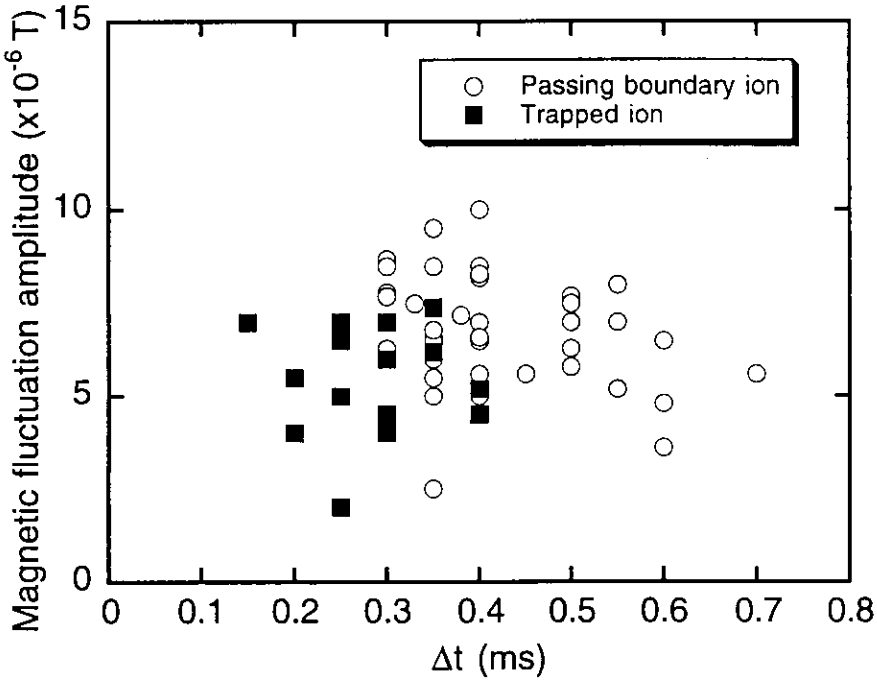

Fig. 47. Correlation between the time from the start of a burst to the start of ejection, Δt and the magnetic fluctuation amplitude when the fast ion ejection starts.

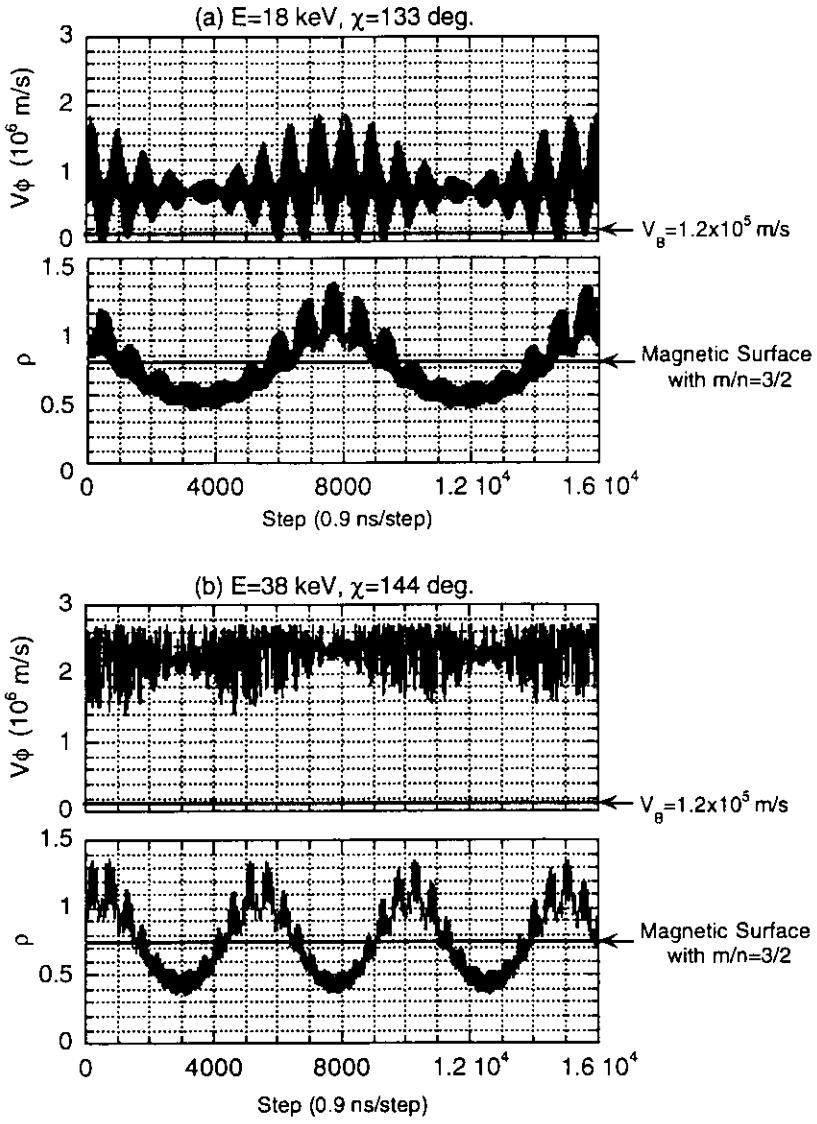

Fig. 48. Variation of the toroidal velocity, V_ϕ and the position represented by normalized minor radius, ρ of an ion on orbit calculation for (a) a passing boundary ion, (b) a passing ion. The phase propagation velocity observed in the magnetic fluctuation was, $V_B = 1.2\text{x}10^5$ m/s, in this case and is presented as a line in the graph of V_ϕ. In the variation of V_ϕ for (a), there are points where $V_\phi$of the passing boundary ion is close to V_B near the magnetic surface with m/n =3/2 when the ion has large pitch angle, V_ϕ~0. Same calculation for the passing ion, (b) shows that V_ϕ does not match V_B although the ion passes through the magnetic surface with m/n =3/2.

Chapter 6

Conclusions

Direct measurements of escaping fast ions by using the scintillator-type lost-fast-ion probe which provides the information on the pitch angle and the energy of detected fast ions have been carried out for the first time in CHS heliotron/torsatron. Loss orbits were identified by using the orbit code. The time behavior of escaping fast ions has been investigated by using this fast measurement to understand the loss processes and the loss mechanisms in heliotron/torsatron devices. The classical loss processes (the prompt loss and the collisional pitch angle scattering loss) and the loss mechanism of MHD-induced loss were experimentally studied.

In classical losses, the signal intensity of passing boundary ions was most intense. For MHD-induced loss, it was observed that co-going passing boundary ions and ctr.-going trapped ions with the energy lower than injection energy were lost periodically correlating with the m/n=3/2 fishbone like instability. The loss rate of passing boundary ions was 10 times larger than that of ctr.-going trapped ions.

Losses were enhanced with increase of the mode amplitude of the instability and there is a threshold in the mode amplitude. The threshold depends on the magnetic structure and the field strength. Analyses to interpret the density dependence and the NB power dependence of losses were made and a simple interpretation that losses depend on accumulation of beam ions in plasmas was given.

With regard to the mechanism of MHD-induced loss for passing boundary ions, it was found that passing boundary ions have resonance points near the m/n=3/2 surface, where their toroidal velocity is close to zero or close to the propagating velocity of magnetic fluctuation. The observed fishbone frequency at the particle ejection time

was close to the estimated toroidal precession frequency of helically trapped ions.

Therefore, it is necessary for future large heliotron/torsatron devices to be cautious in behaviors of passing boundary ions for suppression of energetic ion loss.

References

[1] J. Wesson, Tokamaks second edition, Clarendon Press, Oxford (1997).

[2] M. Wakatani, Stellarator and Heliotron Devices, Oxford Univ. Press, Oxford (1998).

[3] W. W. Heidbrink and G. J. Sadler, Nucl. Fusion **34** (1994) 535.

[4] R. B. White, Theory of Tokamak Plasmas, North-Holland, Amsterdam (1989).

[5] S. J. Zweben, Rev. Sci. Instrum., **57** No.8 (1986) 1774.

[6] S. J. Zweben, Physica Scripta. **T16** (1987) 119.

[7] S. J. Zweben *et al.*, Nucl. Fusion **25** (1989) 825.

[8] S. J. Zweben, Rev. Sci. Instrum., **60** No.4 (1989) 576.

[9] S. J. Zweben *et al.*, Phys. Fluids **B2**(6) (1990) 1411.

[10] S. J. Zweben *et al.*, Nucl. Fusion **30** (1990) 1551.

[11] S. J. Zweben *et al.*, Nucl. Fusion **31** (1991) 2219.

[12] S. J. Zweben *et al.*, Phys. Plasma **1** (1994) 1469.

[13] S. J. Zweben *et al.*, Nucl. Fusion **35** (1995) 893.

[14] S. J. Zweben *et al.*, Nucl. Fusion **35** (1995) 1445.

[15] D. S. Darrow *et al.*, Rev. Sci. Instrum., **66** No.1 (1995) 476.

[16] D. S. Darrow *et al.*, Phys. Plasma **3** (1996) 1875.

[17] D. S. Darrow *et al.*, Nucl. Fusion **36** (1996) 1.

[18] D. S. Darrow *et al.*, Nucl. Fusion **36** (1996) 509.

[19] R. J. Goldstone *et al.*, Phys. Rev. Lett. **47** (1981) 647.

[20] K. Tobita *et al.*, Nucl. Fusion **34** (1994) 1097.

[21] M. H. Redi *et al.*, Nucl. Fusion **35** (1995) 1191.

[22] K. M. McGuire *et al.*, Phys. Rev. Lett. **50** (1983) 891.

[23] W. W. Heidbrink *et al.*, Phys. Rev. Lett. **53** (1984) 1905.

[24] W. W. Heidbrink *et al.*, Phys. Rev. Lett. **57** (1986) 835.

[25] R. Kaita *et al.*, Phys. Fluids B2 (1990) 1584.

[26] K. Matsuoka *et al.*, Proc. 12 th Int. Conf., Nice, IAEA-CN-50/C-I-6, Vol. 2, (1988) 411.

[27] R. H. Huddlestone and S. L. Leonard, Plasma Diagnostic Techniques, Academic Press, New York London (1965).

[28] I. H. Hutchinson, Principle of Plasma Diagnostic, Cambridge Univ. Press, Cambridge (1987).

[29] M. Takechi *et al.*, Rev. Sci. Instrum., **70** No.1 (1999) 442.

[30] M. Takechi, Ph.D. Thesis, Nagoya University (1999).

[31] Isobe, M., *et al.*, J. of Plasma Fusion Res. SERIES, Vol. **1**, (1998) 366.

[32] D. S. Darrow *et al.*, to be published.

[33] W. W. Heidbrink, Ph.D. Thesis, Princeton University (1984).

[34] A. Fujisawa *et al.*, Phys. Plasma **4** (1997) 1357.

[35] H. Sanuki *et al.*, Phys. Fluids B**2** (1990) 2155.

[36] D. S. Darrow *et al.*, J. of Plasma Fusion Res. SERIES, Vol. **1**, (1998) 362.

[37] T. Kondo *et. al.*, in Proc. 1998 ICPP & 25 th EPS Conference on Controlled Fusion and Plasma Physics, F072PR (1998) 1462.

[38] M. Tuszewski and S. J. Zweben, Rev. Sci. Instrum., **63** No.10 (1992) 4542.

[39] D. S. Darrow *et al.*, Rev. Sci. Instrum., **70** No.1 (1999) 838.

[40] S. Sakakibara *et al.*, J. Phys. Soc. Jpn., 63 No.12 (1994) 4406.

[41] T. Kondo *et. al.*, in Proc. 6 th IAEA Technical Committee Meeting on Energetic Particles in Magnetic Confinement Systems (1999) 93.

[42] T. Kondo *et. al.*, accepted for publication in Nucl. Fusion.

[43] K. Toi *et al.*, Proc. 17 th Int. Conf., Yokohama, IAEA-CN69/EXP1/19.

[44] S. Lee *et al.*, J. of Plasma Fusion Res. SERIES, Vol. **1**, (1998) 273.

[45] M. Isobe *et al.*, Rev. Sci. Instrum., **70** No.1 (1999) 827.

[46] D. S. Darrow *et al.*, in Proc. 6 th IAEA Technical Committee Meeting on Energetic Particles in Magnetic Confinement Systems (1999) 81.

[47] R. B. White *et al.*, Phys. Fluids **26** (1983) 2958.

[48] H. Idei *et al.*, Phys. Rev. Lett. **71** (1993) 2220.

[49] M. Isobe *et al.*, in Proc. 26 th EPS Conference on Controlled Fusion and Plasma Physics, OR06 (1999) 21.

[50] W. H. M. Clark *et al.*, Phys. Rev. Lett. **45** (1980) 1101.

[51] L. Spitzer, Jr., Physics of Fully Ionized Gases, Interscience, New York (1962).

[52] Chen, L., White, R. B. and Rosenbluth, M. N., Phys. Rev. Lett. **52** (1984) 1122.

[53] Coppi, B. and Porcelli, F., Phys. Rev. Lett. **57** (1986) 2272.

[54] Betti, R and Freidberg, J. P., Phys. Rev. Lett. **70** (1993) 3428.

[55] Miyamoto, K., Plasma Physics for Nuclear Fusion, MIT press., Cambridge, Mass. (1980).

[56] M. Takechi, *et. al.*, Phys. Rev. Lett. **83** (1999) 312.